Weiqiang Liu

Experimental and Numerical Analysis of Blast Furnace Drainage

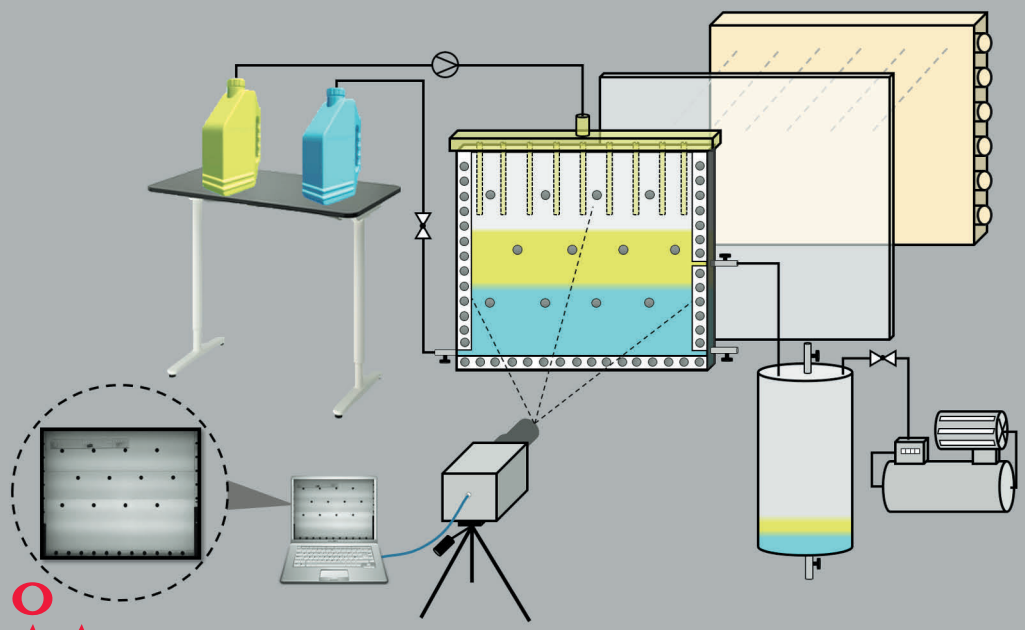

Åbo Akademi University

Weiqiang Liu

Born 1992, Shandong, China

M. Sc. Metallurgical Engineering, 2017
Northeastern University, Shenyang, Liaoning, China

Experimental and Numerical Analysis of Blast Furnace Drainage

Weiqiang Liu

Laboratory of Process and System Engineering
Faculty of Science and Engineering
Åbo Akademi University
Åbo, Finland, 2022

Supervisor

Prof. Henrik Saxén
Faculty of Science and Engineering,
Åbo Akademi University, Finland.

Co-supervisors

Docent Mikko Helle
Faculty of Science and Engineering,
Åbo Akademi University, Finland.

Assoc. Prof. Lei Shao
School of Metallurgy,
Northeastern University, China.

Opponent and Reviewer

Docent Ville-Valtteri Visuri
Outokumpu Stainless Oy/University of Oulu, Finland.

Reviewer

Prof. Pär Jönsson
Department of Materials Science and Engineering,
KTH Royal Institute of Technology, Sweden.

ISBN 978-952-12-4154-3 (printed)
ISBN 978-952-12-4155-0 (digital)
Painosalama, Turku, Finland 2022

Preface

The work reported in this doctoral dissertation was carried out at the Process and Systems Engineering Laboratory, Åbo Akademi University, Finland during 2018-2021. The research was mainly supported by the Graduate School Program of Åbo Akademi University Foundation. I gratefully acknowledge the financial support that enabled me to focus on my thesis work during the four years.

I would very much like to express my sincere thanks to my supervisor Professor Henrik Saxén who always shares his knowledge and gives me positive energy. His guidance and encouragement have been the constant motivation for my thesis work, which also made this thesis possible. I also would like to appreciate my master's thesis supervisor, Associate Professor Lei Shao, for all of his help. His encouragement has given me enough courage and confidence to pursue the doctoral degree and finish my thesis work.

I would like to thank Professor Ron Zevenhoven, Docent Frank Pettersson, Dr. Mikko Helle for your valuable courses. I would like to thank Affi who supported me and guided my experiments. Thank you to Vivéca for the office-related and administrative help. A special thanks to Debanga for the help during the thesis work and daily life. I also want to thank the former and present colleges (Anders, Annika, Javier, Markéta, Calle, Umara, Jeffery, Gopalakrishna, Han, etc.) at the laboratory for enjoying lunches and coffee breaks together.

I would like to express my thanks to all of my friends in Finland and China who have ever accompanied and helped me throughout these years. I also wish to thank my girlfriend Hua for all the love and trust. Finally, I want to express my grateful thanks to my parents for their unconditional love and support.

Turku/Åbo, Feburary 2022

Weiqiang Liu

Abstract

The thesis studies slag and iron flow in the blast furnace hearth and the complex hearth drainage phenomena by both experiments and numerical simulation. It also presents a mathematical model by which the asymptotic state of the hearth lining can be estimated. The main points of the work were to undertake a quantitative analysis to shed further light on blast furnace hearth drainage and the corresponding flow and behavior of the interfaces. A transparent Hele-Shaw (H-S) slot model was constructed and experiments were undertaken with it. To gain quantitative tapping information from the experimental model, an image analysis algorithm was developed to treat and refine the experimental results. The H-S model has inherent merits for the application of image analysis, such as low optical distortion. Based on the developed image analysis method, the role of the blast pressure, slag viscosity, and initial accumulated liquid amounts on the tapping duration and residual liquid ratios were examined. Some results were processed to dimensionless form to employ the findings in the practical BF system. In addition, the influence of the operational conditions on the tapping end state was studied. The evolution of liquid levels and volumes, liquid outflow rates and oil ratio, as well as interface angles was studied to characterize the hearth draining.

Since it is not easy to use the H-S model to study certain factors, like the coke-free zone or bed permeability, a simulation model of the H-S was developed to mimic the experimental counterpart. This computational fluid dynamics (CFD)-based model was first validated by experimental data and then applied to analyze the evolution of key process variables. Even though the real furnace hearth experiences continuous inflows of iron and slag, the experiments and computational models developed in this thesis for the sake of simplicity only considered the drainage. To gain an understanding on how the hearth lining design and boundary conditions affect the inner profile of the hearth, an asymptotic erosion model was also developed. The model considers hot metal flow, heat transfer, lining erosion, and possible skull formation and can be used to estimate the durability of the hearth. A number of cases were studied to illustrate the applicability and versatility of the model.

Abstrakt

Denna doktorsavhandling studerar strömningen and järn och slagg i masugnens nedersta del, s.k. ställ, och den komplexa dräneringen av ugnen under tappning. Forskningen baserades på såväl experiment i liten skala som numerisk simulering. I arbetet utvecklades även en matematisk modell för ställväggens och -bottnens slutliga tillstånd för en specifik ställdesign samt drifttillstånd hos masugnen.

Doktorsarbetets huvudsakliga avsikt var att undersöka förhållandena under tappning av masugn och att kvantifiera hur de två smälta faserna flödar ut ur ugnen. Speciell tonvikt sattes vid hur gränsskikten mellan fluiderna utvecklades under tappningen. En genomskinlig spaltmodell, av H-S-typ, byggdes och användes i arbetets experimentella delar. I laboratoriemodellen ersattes järn och slagg av vatten och olja, som inbördes visades ha sådana egenskaper att slutsatser om det verkliga systemet kunde dras på basis av experimenten.

För att kunna behandla stora datamängder samt erhålla tillförlitlig information från spaltmodellens försök utvecklades en metodik för automatisk bildanalys, som via videosekvenser kan detektera fasernas gränsskikt och därför beskriva dessa numeriskt för vidarebehandling av informationen. Metoden möjliggjorde även en automatisk uppföljning av vätskevolymerna i H-S-modellen under experimenten, vilket implicit även gav utflödeshastigheterna av vatten och olja. På basis av metoden studerades inverkan av blästertryck, slaggviskositet och startvolymerna av järn och slagg i masugnsstället på tapptiden genom motsvarande försök i H-S-modellen, där resultaten för vatten och olja omformades med hjälp av dimensionslösa uttryck så att slutsatser beträffande de industriella förhållandena kunde dras. Försöken gjordes utan att tillföra vätskor, vilket betyder att endast dräneringen (utflödet) beaktades i experimenten. Med modellen studerades bl.a. hur omständigheterna påverkade de slutliga vätskemängderna, hur vätskenivåerna och –utflödet utvecklades samt hur, och i vilken omfattning, gränsskikten deformerades i närheten av tapphålet under tappningens gång. Arbetet klargjorde de faktorer som ha stor betydelse för tappningsförloppet, samt illustrerade även möjliga avvikande tillstånd som kan uppstå under vissa omständigheter. Blästertrycket befanns spela en avgörande roll vid dräneringen för både tappningshastigheterna och restvolymerna av smältorna då tappningen avslutats. Ett exempel ur avvikande tillstånd är tappningar som slutar fastän gränsskiktet mellan järn och slagg överlag befinner sig ovanom tapphålets nivå.

Då det inte var enkelt att studera vissa parametrar med den experimentella modellen, såsom t.ex. bäddpermeabiliteten eller en möjlig

flytning av koksbädden i masugnen, utvecklades även en numerisk modell på basis av strömningsmekanik (eng. computational fluid dynamics, CFD) för H-S-systemet. Den numeriska modellen efterliknar det experimentella systemet och kan användas för jämförelse samt för att analysera variabler vilkas värden inte kan ändras i laboratoriemiljö. Modellen befanns beskriva den experimentella modellen med acceptabel noggrannhet och utnyttjades därefter för att teoretiskt studera vissa faktorers inverkan på dräneringsförloppen. I överensstämmelse med resultat som rapporterats i litteraturen fann man att utströmningen av vätskorna påverkades kraftigt av en koksfri zon i bädden som sträcker sig ända upp till tapphålet.

I praktiken är masugnsställets dimensioner inte statiska utan förändras under driften p.g.a. slitage av de eldfasta ställmaterialen samt även av möjliga ansättningar av material på ställväggen och –bottnen. För att öka förståelsen för hur ställdesign samt driftsparametrar, såsom omständigheterna vid ställets gränser, påverkar förloppen utvecklades en matematisk modell som beskriver det asymptotiska sluttillståndet för ställinfodringen. Modellen, som är två-dimensionell och statisk, beaktar strömningen av järnsmältan, värmeöverföring från smältan via ställväggen och –bottnen till omgivningen, och estimerar samtidigt infodringens slitaget samt möjlig bildning av ansättningar. Den kan därför användas som ett verktyg för att teoretiskt studera hur ställdesign (geometri, materialval) samt driftomständigheter (produktionstakt, väggkylning, etc.) påverkar det förväntade fortfarighetstillståndet hos stället. Ett flertal intressanta fall studerades med modellen för att belysa dess användningsmöjligheter.

List of publications and contribution of the author

The following five publications form the basis of this thesis and are included in the thesis as appendices:

I. Liu, W., Mondal, D. N., Hermanson, A., Shao, L. and Saxén, H. (2021). An image analysis-based method for automatic data extraction from pilot draining experiments. *Ironmaking & Steelmaking*, vol. 48, pp. 263-274.

II. Liu, W., Shao, L. and Saxén, H. (2020). Experimental Model Study of Liquid–Liquid and Liquid–Gas Interfaces during Blast Furnace Hearth Drainage. *Metals*, vol. 10, 496.

III. Liu, W., Shao, L. and Saxén, H. (2021). Experimental Study of Blast Furnace Hearth Drainage Based on Image Analysis. *Steel research international*, vol. 92, 2100142.

IV. Liu, W., Shao, L. and Saxén, H. (2022). Numerical Analysis of Blast Furnace Hearth Drainage Based on a Simulated Hele-Shaw Model. *Steel research international*, accepted, doi: 10.1002/srin.202100629.

V. Liu, W., Shao, L. and Saxén, H. (2022). Asymptotic Model of Refractory and Buildup State of the Blast Furnace Hearth. *Metallurgical and Materials Transactions B*, vol. 53, pp. 320-333.

The author of the thesis is the main contributor to all publications. He has conducted all the experiments and simulation investigations about the hearth drainage in Papers I-IV. The hearth erosion model (in Paper V) was developed with expert counseling from Henrik Saxén and Lei Shao. The author was responsible for writing the draft of each paper and later revising the draft with the supervisors.

Table of contents

1. Introduction

Steel is one of the most important multi-purpose materials in the world used for a variety of purposes and products. It has played a central role for the development of mankind. Steel can be infinitely recycled and reused, so is an essential material for a successful circular economy. It is also broadly applied in many fields, ranging from infrastructure and housing to manufacturing and diverse steel products, which shows its close relation to modern life (www.worldsteel.org). The steel demand in the world has shown an increasing trend and the global production of crude steel also has grown considerably from 1950 to 2020, particularly so in the 21st century (Figure 1, www.worldsteel.org).

The pig iron is the main raw material for steelmaking and is produced primarily by two routes: smelting reduction (SR) and direct reduction (DR) (Seshadri, 2014). As the core equipment of the SR route, the blast furnace (BF) is the dominating unit. It has existed and been developed for a few hundred years and it supplies about 70% of the pig iron used for steelmaking (www.worldsteel.org). Even though new ironmaking techniques have appeared and are being developed, like the Corex process, most of them are still not economically competitive compared to the BF for large-scale production. Despite the present view that the carbon-based steelmaking must be replaced by alternative, more sustainable technologies, such as hydrogen-based direct reduction furnaces, it is still safe to assume that the BF will maintain its predominant role as an iron producer to support large-scale steelmaking in the coming decades.

To keep the competitive position of the BF and to simultaneously reduce its carbon dioxide emissions, continued efforts have to be made to develop and improve the overall performance of the BF, e.g., in terms of higher production rate, lower reductant rate, and longer campaign life (Shao, 2013). The lowermost part of the BF, the hearth, is the heart of the system and a stable hearth state is a prerequisite for a smooth and efficient BF operation as well as a long campaign life. A well-controlled drainage is a key issue for a stable hearth state, because a non-smooth hearth drainage causes uncontrolled fluctuations in the levels of liquids in the hearth, which may lead to an unstable burden descent and gas permeability problems, which disturb the entire BF operation (Roche, 2020). This is the reason why many researchers have studied various problems and aspects of the BF hearth by different methods, including physical experiments and numerical simulations, to gain an understanding of the complex hearth phenomena. However, more investigations are still needed to get a deeper understanding of the hearth drainage especially to gain a more detailed and quantitative view of the drainage process. This is one of the main motivations behind the presented thesis work.

The operation of the BF hearth also affects the state of the lining. Since large hearth refractory repairs cannot be undertaken without a full stoppage and complete emptying of the furnace, the BF campaign is limited by the hearth life length (Cameron et al. 2020). To gain an understanding of the factors that affect the wear of the hearth refractories, a large number of mathematical models have been developed. Most models have focused on estimating the present wear of an operating BF, based on thermocouple signals from the lining, while models simultaneously considering both liquid flow and lining state are scarce (Brännbacka and Saxén, 2008). This lack was addressed in the thesis by developing a model of the asymptotic lining state of a hearth of a given design operated under specific boundary conditions.

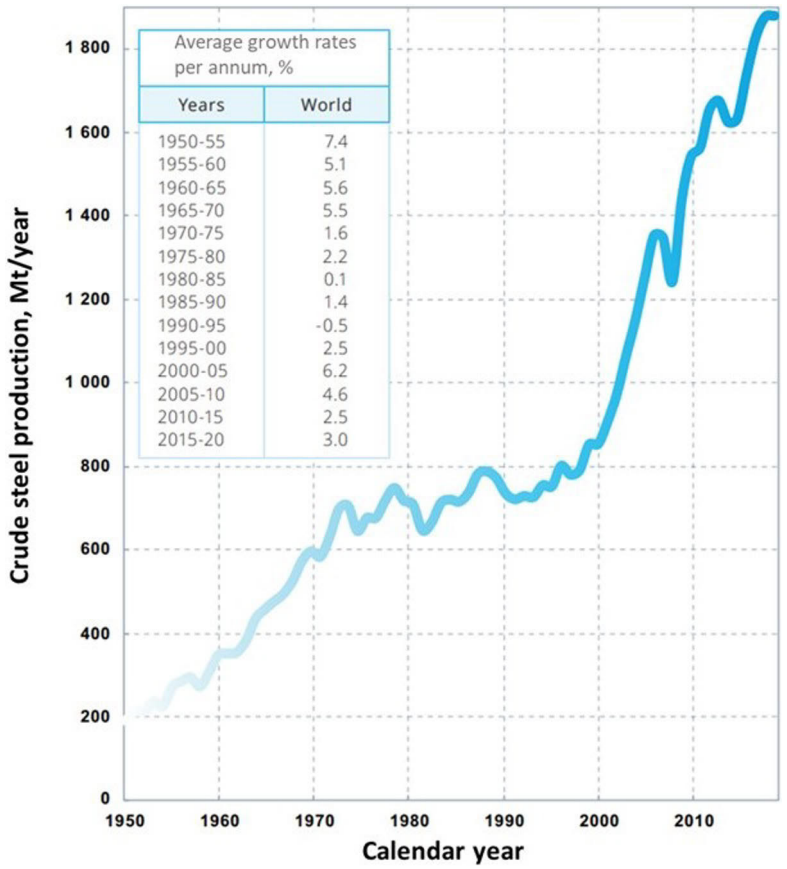

Figure 1. *Total global production of crude steel from 1950 to 2020 (Data Source: www.worldsteel.org).*

Based on the motivations above, the main research questions of the present thesis were:

Q1) Is it possible to gain useful information about blast furnace tapping by cold model experiments in the laboratory?
Q2) How can results from such experiments be captured reliably and consistently by measurements?
Q3) Is it possible to develop a computational counterpart that can reproduce the experiments and extend the analysis to study the effect of variables that cannot be varied in the laboratory experiments?
Q4) Can the blast furnace hearth wear be estimated by a CFD model that considers simultaneous fluid flow, heat transfer, refractory erosion, and skull formation?

Research question Q1 is addressed in Papers II and III, which describe the development and application of a laboratory-scale Hele-Shaw slot model that studies drainage of two liquid phases. The work studies the tapping behavior with respect to residual liquid ratios, tapping end states, the evolution of the liquid levels and volumes, outflow rates and oil ratio, as well as interface angles during the tapping. Paper I mainly addresses Q2. It demonstrates that an image analysis-based method can be successfully applied to make quantitative analyses of the tapping experiments after solving a set of problems that arises from the treatment and compilation of the visual information. Paper IV focuses on research question Q3 and addresses drawbacks of the experimental method by developing a computational counterpart, which makes it possible to study the effect of an extended set of variables. Finally, research question Q4 is tackled in Paper V, where a CFD model is developed to consider fluid flow, heat transfer, refractory erosion, and skull buildup simultaneously in one computational domain. The paper outlines the general structure and solution procedure of the model and demonstrates its applicability and versatility to studying the expected asymptotic wear of blast furnace hearths of different designs and operated under different conditions.

The brief summary of the thesis that follows provides a basic introduction to the field. Various studies about the BF hearth and hearth drainage are reviewed, especially focusing on the literature closely related to the focus of the present work. Finally, the methods applied and the main findings of the thesis are presented, followed by a section where conclusions are drawn.

2. Blast furnace and its operation

This chapter briefly introduces the BF ironmaking process, paying particular attention on the hearth region and its operation.

2.1. Overview of the blast furnace ironmaking process

A BF is an efficient large-scale countercurrent chemical reactor and heat exchange apparatus with a remarkable extent (85-90%) of heat utilization (Biswas, 1981). Complex chemical reactions, heat exchange, and mass transfer occur in the BF when iron-bearing minerals are reduced to molten iron for further processing in the downstream steelmaking process.

The BF includes multiple sections (or zones), i.e., throat, shaft, belly, bosh, and hearth (Figure 2, Geerdes et al. 2015). The furnace geometry and dimension in each zone are decided by the furnace working methods, operational conditions, burden materials, etc. The furnace design should promote a smooth burden descent and a uniform ascent of gases, distributing over the whole furnace cross-section. The iron-making raw materials, i.e., iron ore, coke, and flux, are charged from the top part of the furnace through the charging system. During the charging, the coke and iron ore (with flux) dumps are charged separately, forming coke and ore layers which generate a layer-structured burden (Shao, 2013). The ores are heated and reduced gradually by the ascending hot reducing gas during the burden descent and at some point this material starts softening and melting in a region called the cohesive zone.

The hot reducing gas is generated in the lower part of the furnace, the furnace bosh. Here, the hot air enriched with oxygen and auxiliary fuels (like pulverized coal or natural gas) is blown into the furnace via a group of channels distributed around the BF peripheral and through a set of nozzles, named tuyeres. The coke particles that descend from the cohesive zone and the auxiliary injected fuels combust with the blast air in front of the tuyeres to supply the energy and reducing gas for the BF system in a local hollow space, raceway, formed in front of the tuyere (Geerdes et al. 2015). The use of auxiliary fuels, such as pulverized coal, can reduce the consumption of the expensive coke, but the amount of auxiliary reductant should be controlled carefully to avoid problems of reduced bed permeability or incomplete conversion of the reductant. The generated reducing gases (carbon monoxide and hydrogen) flow upwards through the dribbling zone, pass through the cohesive zone via the coke slits and then flow through the shaft section, heating and reducing the descending solids. The distribution of the ascending gas in the shaft and throat depends on the cohesive zone shape, which, in turn, depends on the burden distribution (and mainly the radial ore-to-coke ratio). An overall

uniform reducing gas distribution over the shaft cross-section is preferred for achieving a high heat and gas utilization. Finally, the gas reaches the top part of the furnace and flows out through the gas uptakes.

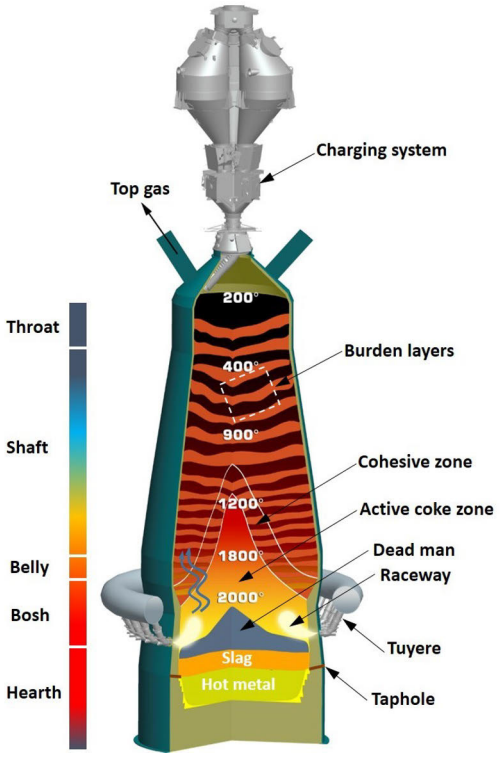

Figure 2. *Schematic of the blast furnace unit and its charging system (Geerdes et al. 2015).*

Below the cohesive zone, the molten iron and slag droplets trickle down through the active coke zone and the stagnant packed coke bed (dead man), and then accumulate in the furnace hearth as two separated layers, with the lighter slag floating upon the heavier iron. When the accumulated liquids (are estimated to) reach a certain level inside of the hearth, the taphole on the sidewall is opened by drilling, so the molten iron and slag can be drained. The hearth drainage is ended by plugging the taphole using the taphole mud. This intermittent draining procedure is normally repeated 10-12 times per day.

2.2. Burden charging, burden distribution and gas flow

A rational gas flow is essential to achieve a stable and efficient BF operation. For the BF system, controlling burden distribution is the main way to manage the BF ascending gas flow. The burden distribution is the result of the alternative charging of the different burden materials (i.e., coke and iron ore with flux) by the BF charging system.

Before the 1970s, the two-bell charging system was used for BF charging. Since engineers from Paul Wurth developed a rotating chute (bell-less) charging system, it has dominated almost all new blast furnaces (Cameron et al. 2020). A schematic of two kinds of charging systems is shown in Figure 3 (Cameron et al. 2020). Compared to the bell charging system, the bell-less system can achieve a very flexible burden distribution, which can assign different burden materials anywhere on the stockline. The burden charging will start when the burden descends to the level below the stockline, which is measured by radar. In general, the burden descends smoothly but sometimes the non-normal burden descending also happens such as burden hanging (little or no burden descent) and burden slips (fast and uncontrolled burden descent). Such abnormal descending phenomena disturb the gas flow and cause adverse effects for the BF operation. To study and improve the burden distribution, many charging models based on DEM and fast mathematical calculations have been established (Mitra and Saxén, 2014; Park et al. 2011; Fu et al. 2015; Chibwe et al. 2020).

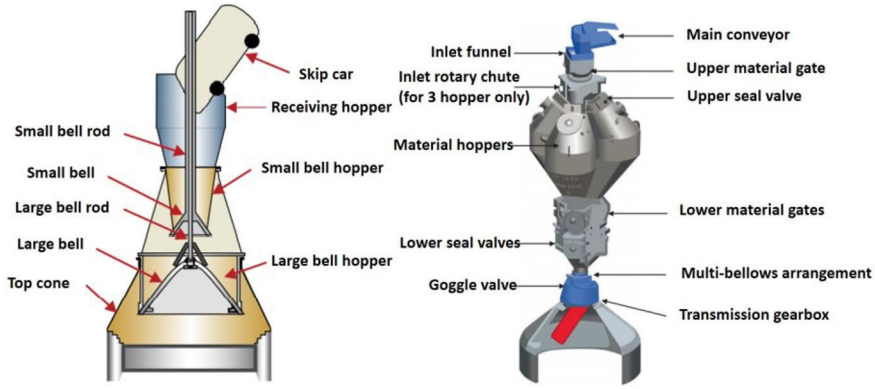

Figure 3. *Schematic of blast furnace charging systems. Left panel: two-bell charging system. Right panel: bell-less charging system with three hoppers (Cameron et al. 2020).*

After the charging, a layer-structured burden is formed in the shaft. Because the coke is much larger than the pellet (or sinter), the coke layer has a higher permeability, so the gas flow can be controlled by managing the radial distribution of the ore-to-coke (O/C) ratio. There are two basic types of gas distribution for the BF: central working furnace and wall working furnace, which can be achieved by different burden distribution patterns.

For a central-working furnace, the center part of the furnace is only occupied by the coke. A schematic of the central working furnace and the corresponding burden distribution in the throat is illustrated in Figure 4 (Geerdes et al. 2015). It shows that the central gas flow is the dominant and the gas is distributed through the coke windows from the furnace center to the peripheral side. This gas-flow pattern is the result of the decreasing ore-to-coke ratio from the furnace wall to the center, which forms an inverted "V"- or even inverted "U"-shaped cohesive zone. The opposite operation state is the wall-working furnace (Figure 5, Geerdes et al. 2015). It shows that the ore-to-coke ratio in the throat is relatively uniform, forming a "W"-shaped cohesive zone. The softening and melting iron ore in the furnace center constrains the center gas flow and directs the gas towards the peripheral area.

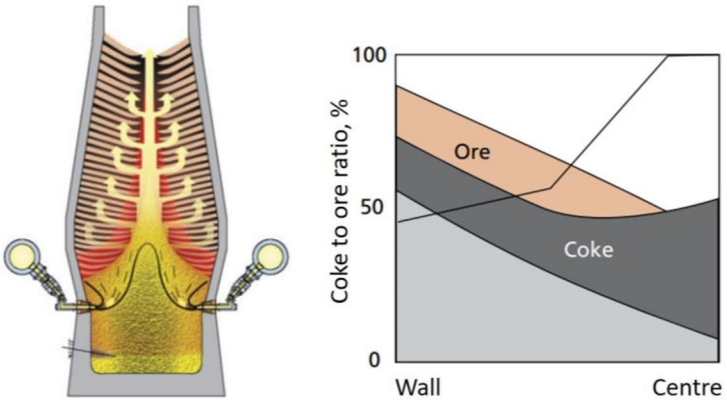

Figure 4. *Schematic of a central-working furnace (left panel) and the burden distribution in the throat (right panel) (Geerdes et al. 2015).*

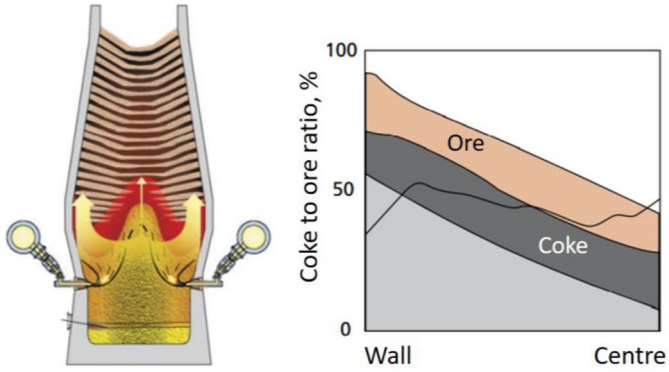

Figure 5. *Schematic of a wall-working furnace (left panel) and the burden distribution in the throat (right panel) (Geerdes et al. 2015).*

The central-working BF is known to generally run with stable and good performance, characterized by high productivity and good hot metal quality. However, it has some drawbacks, e.g., a relatively low root of the cohesive zone which may could disturb the furnace permeability, and also cause problems at disturbances. For the wall-working furnace, the root of the cohesive zone is higher, which gives some margin of operation, but this state has some other problems. A main problem is the severe heat losses caused by the strong gas flow close to the wall, which can raise the fuel rate. In addition, it also intensifies the refractory wear or may even destroy the cooling system in the shaft. Considering both cases, an ideal burden distribution should be one case where coarse coke is charged in the furnace center to ensure the dominant center gas flow and some nut coke also need to be charged in the wall area to lower requirements of the heat and reduction gas near the wall area.

2.3. Cohesive zone, dribbling zone and raceway

During the burden descent, the iron-bearing materials are heated and reduced gradually by the ascending hot gas. When they are heated up to around 1100 °C, the indirect reduction of iron-bearing materials is almost finished, and gradually soften and slag separation starts in the upper part of the cohesive zone. The burden compresses the softening iron-bearing materials in rings while slag is squeezed out. The coke layers between the metal rings remain practically intact and work as paths for the ascending gas flow; these are often named coke slits or coke windows. With the hot gas flowing through the coke slits, the metal is further heated, and when its temperature exceeds 1200 °C, the metal melting begins, which forms the lower boundary of the cohesive zone. The cohesive zone thus consists

of a softening and gradually melting metal layer and coke layer with alternative distribution (cf. Figure 2 of Geerdes et al. 2015). A typical profile of the cohesive zone is of inverted V shape and the root of the zone is generally located in the bosh.

The dripping zone is the space under the cohesive zone where the molten iron and slag droplets drip down, passing through the voids between the coke particles, and finally enter and accumulate in the hearth. The iron and slag droplets are diverted by the strong gas flows from the raceways when they are passing the tuyeres level.

The raceways are a group of cavities which form in front of the tuyeres when the hot blasts injected through the tuyeres results in combustion of coke and injected reductants. The coke particles, supplied from above primarily from the active coke zone (Omori 1987) between the lower boundary of the cohesive zone and the upper boundary of the stagnant coke region (dead man, cf. next subsections), circulate and crumble in front of the tuyeres during the combustion process. Finally, small particles are accumulated in the deeper locations of the raceway and are combusted when the new coke enters in the cavity. These fines may also partially clog the back boundary of the raceway, forming a region called "bird's nest" (Shen et al. 2014).

2.4. Hearth and hearth linings

The hearth, located in the lowest section of the BF, works as a temporary storage of molten iron and slag (cf. Figure 2, Geerdes et al. 2015). Below the active coke zone, a packed coke bed, the dead man, is the only material in solid form. From here onwards, the term dead man and hearth coke bed are used as synonyms, even though the former sometimes is used only to refer to the core of the latter. The voidage of the dead man is generally assumed to be between 0.3 and 0.5 (Kanbara et al. 1977), which indicates that only 30-50% of the hearth volume is available for the hot metal and slag in the case with a sitting dead man.

The hearth represents a high-temperature zone, so it is necessary to use refractory materials to line the region (Figure 6, Houde et al. 2013). The environment is extremely hostile with flows of hot, molten materials, chemical reactions, mechanical wear, dissolution of components into the hearth liquids, etc. Thus, it is unavoidable that lining erosion occurs. A strong hearth erosion leads to the need of hearth repairs and relining, which is the most expensive maintenance activity for the whole BF. In addition, long BF stoppages are also needed for the hearth maintenance, which disturbs the hot metal production and further increases the economic costs. In case of sudden and severe erosion, a breakout can occur, where hot metal (and slag) flow out uncontrolled. This is one of the

main disturbances in the BF operation and it can have serious economic and safety consequences. Therefore, it is essential to optimize the lining design and to control the internal conditions in the hearth to extend the campaign life.

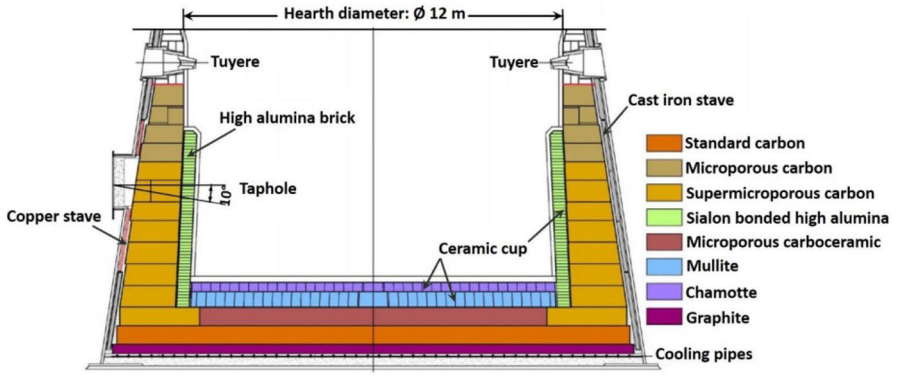

Figure 6. *Industrial blast furnace hearth and lining design (Houde et al. 2013).*

Different refractory materials (like carbon, graphite, mullite) are used in the different locations of the hearth structure to better exploit their advantages. For instance, the microporous (or super-microporous) carbon bricks with superior thermal conductivity are installed in the region close to the taphole to efficiently remove the local high heat load and extend the lining life. Some water cooling elements such as cooling staves and plates are also integrated into the lining to enhance the cooling efficiency. The metal materials used for the cooling elements are also different; most commonly copper and cast iron are chosen. A schematic of the installation and application of different cooling elements is depicted in Figure 7 (Geerdes et al. 2015). Except for the design optimization of the lining integrated with coolers, controlling the protective buildup, i.e., skull, formation on the hot face of the lining to isolate the lining from liquids is another strategy for lining protection.

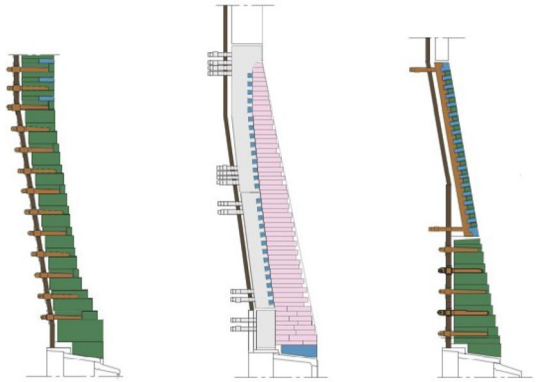

Figure 7. *Schematic of the installation and application of different cooling elements. Left panel: plate coolers. Middle panel: stave coolers. Right panel: hybrid coolers (Geerdes et al. 2015).*

To maintain the stable and efficient hot metal production, simultaneously not endangering the campaign life of the BF, a reliable and timely monitoring and assessment of the hearth lining status and thickness is crucial. There are two main ways, i.e., a direct and indirect one, that have been applied to determine the lining status of the BF. The direct measurement is the most accurate approach but it cannot be used when the furnace is running. During BF relining and maintenance, the lining condition and thickness can be assessed directly by careful drilling and sampling from the refractory lining in the different regions of the hearth. After drilling, the remaining lining thickness is known and the samples can be analyzed to determine changes of the lining composition and state. However, ideally, the BF operators should always know the lining thickness and status of the operating furnace to take appropriate control actions. Therefore, online techniques are necessary to estimate the lining thickness of a running BF. A relatively mature method is to apply inverse heat conduction models to estimate the lining profile and thickness based on the temperature readings from the thermocouples in the hearth lining. This type of models has been developed by different researchers (Torrkulla and Saxén, 2000; Gonzalez and Goldschmit, 2006; Brännbacka and Saxén, 2008). The main drawback of the method is its accuracy heavily depends on the number and distribution of the installed thermocouples as well as the precision of the thermocouple readings and the accuracy of the values of the thermal conductivity of the lining materials. Other indirect methods also reported and tested are based on infrared thermography, acoustic emission, etc. (Bolf, 2004; Cameron et al. 2020).

2.5. Dead man dynamics

The stagnant coke packed bed was named the dead man because it was earlier (incorrectly) taken to be an inactive part in the lower zone of the furnace (Nishio et al. 1977). However, the dead man is gradually consumed in the furnace because of the carbonization of the hot metal, the reduction reactions with some oxides like FeO, and the consumption by combustion in the raceways. The descending coke especially in the center of the furnace acts as the source for the dead man renewal. A full renewal of the dead man has been claimed to require a few weeks, but it is believed that a faster renewal occurs in the peripheral area due to a stronger local liquid flow. The permeability of the dead man is likely to be heterogeneous, which is attributed to the non-uniformly distributed renewal process caused by the spatially varying liquid flow and heat transfer in the hearth (Sugiyama 1996). Some industrial trials have been conducted by applying radioactive tracers to study the dead man permeability and it shows the dead man core is more impermeable (Negro et al. 2001).

The position and the bottom shape of the dead man in the hearth change dynamically during the furnace operation and is related to the force balance on the dead man and liquid levels of the hearth. The forces acting on the dead man are the integrated downward forces (e.g., the gravity of the burden column and the holdup of dribbling liquids reduced by the drag of the ascending gas and the friction of the wall) and the buoyancy of the liquids (iron and slag) in the hearth. The liquid levels in the hearth depend on the balance of the accumulation and drainage of the molten iron and slag, so they also vary dynamically. In addition, the above-mentioned gas drag acting on the dead man is gradually decreased from the peripheral of the dead man to the center. Considering this, the dead man state has generally been classified into four categories: completely sitting, completely floating with a flat bottom, completely floating with a higher level close to the wall, and partly floating near the wall, as shown schematically in Figure 8. Thus, the dead man floating state may vary during the furnace operation along with changes in the liquid levels, blasting conditions, and burden distribution. As the molten iron exerts a stronger buoyancy than slag because of its higher density, the dead man state heavily relies on the sump depth, i.e., the distance between the hearth bottom and the entrance of the taphole (Andreev et al. 2017). As it is not feasible to measure or monitor the dead man state directly, simplified physical models and mathematical models have been developed to investigate the dead man dynamics (Takahashi et al. 2002).

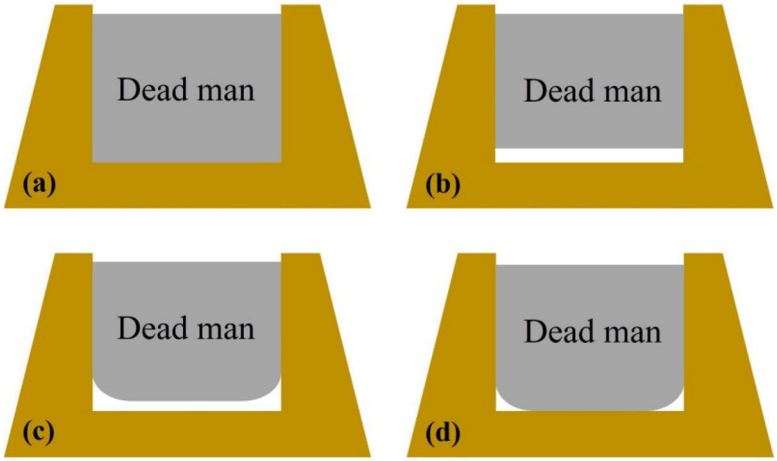

Figure 8. *Different dead man floating states in the blast furnace hearth. (a) sitting, (b) floating with horizontal bottom, (c) floating with a higher floating level at the wall, and (d) partially floating.*

The dynamic dead man state is closely related to the liquid flow and hearth lining erosion. For a floating dead man, a coke-free zone exists under the dead man, which affects the liquid flow path significantly. A partly floating dead man causes an intensive circumferential flow and a flow-induced shear stress on the lining in the area between the hearth sidewall and the bottom. This is assumed to be the primary cause of an "elephant-foot-shaped" erosion profile reported for many furnaces after the campaign. A "bowl-shaped" erosion profile is also possible and is likely to arise in the case of a completely sitting dead man. To study the effect of the dead man floating state on the flow-induced shear stress, Shao and Saxén (2012a) established a CFD model. An example of the arising shear stress distribution on the hearth bottom is shown in Figure 9 (Shao and Saxén, 2012a). These findings indicate that a fully floating dead man could relieve the shear stress to some extent since a quite uniform shear stress distribution is seen to develop.

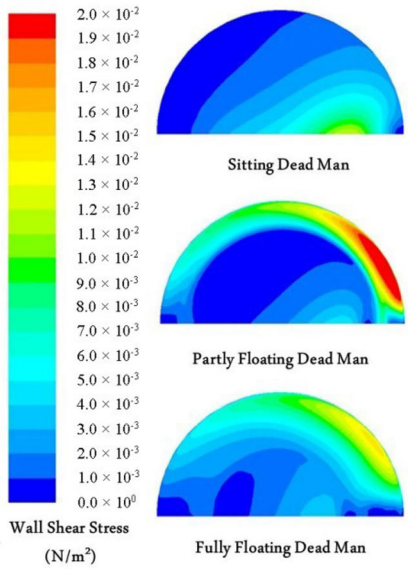

Figure 9. *Shear stress distribution on the hearth bottom for the different dead man floating states (Shao and Saxén, 2012a).*

2.6. Hearth drainage

The hearth drainage, or tapping, of the BF is the process to extract the accumulated molten iron and slag from the hearth through the taphole. The taphole is an opening channel drilled through the hearth sidewall and it plays an essential role in the hearth drainage. Smooth drainage is a prerequisite for a stable and efficient BF operation and production because a poor or uncontrolled tapping may cause excessively high liquid level, which disturbs the burden descent and the flow of reducing gas from the raceways. Therefore, it is important to monitor the liquid level inside of the hearth in real time. Gaining the information of the hearth liquid levels in time is also very helpful for the furnace operators to manage the hearth liquid levels by a proper choice of drill rod or for starting or interrupting a tapping. Unfortunately, it is still not feasible to measure the liquid levels inside of the hearth directly due to the extremely hostile conditions in the hearth. To tackle this problem, researchers have developed online tapping models to estimate the liquid levels in the hearth (e.g., Dong and Saxén, 2001; Roche et al. 2019). Such models are based on the process data about the production and the tapping rates, where the former is usually based on material balances for the gas and the latter on the weight of or liquid level in the torpedo/ladle. One inevitable drawback of these models is the data drift caused by the data errors and model simplification, so it is necessary to employ the appropriate filters to correct the drift in order to get realistic estimates of the liquid levels.

The drainage starts as the taphole is drilled and it is ended by injecting clay into the taphole using a mud gun. Small furnaces have only one taphole, so the tapping is not continuous and the time gap between two taps is necessary to allow for the injected taphole clay to solidify properly. This usually causes more notable liquid-level variations in the drainage cycle compared with the situation in a large furnace with (almost) continuous tapping. Middle- and large-size furnaces typically have 2-4 tapholes and two of them are used alternately to achieve a practically continuous tapping (Geerdes et al. 2015). During the drainage, the taphole, and in particular the area near the taphole entrance, is eroded heavily because of the action of the hot and eroding liquids that continuously flow through the taphole. Therefore, at the taphole plugging process an excess of taphole clay is injected to cure and rebuild the taphole. The excess clay will further accumulate around the inner entrance of the taphole to generate a local protective zone (often named mushroom), as shown in Figure 10. The mushroom can extend the taphole further towards the inner parts of the hearth, which promotes liquid flow through the dead man center, restraining circumferential flow. The extended taphole also decreases the tapping rates because the main frictional losses occur here. Thus, the existence of the mushroom is favorable for hearth lining protection and for keeping the dead man center active. Yet another effect of the mushroom is that it is possible to empty the hearth to a lower level since the extended declining taphole lowers the taphole entrance. In practice, it is possible to form the stable mushroom only if the dead man and the injected taphole clay make a good contact close to the taphole inside the opening. This can be achieved by managing the blasting to control the raceway size above the taphole (Tsuchiya et al. 1988). The taphole clay quality is also essential for a stable tapping: high-quality clay has a better durability against the strong thermal and chemical attack as well as the stress exerted by the flowing liquids. This makes it possible to maintain the relatively intact tapping channel during the tapping. The taphole clay can also affect the taphole wall roughness and in this way affect the taphole stream (He et al. 2002).

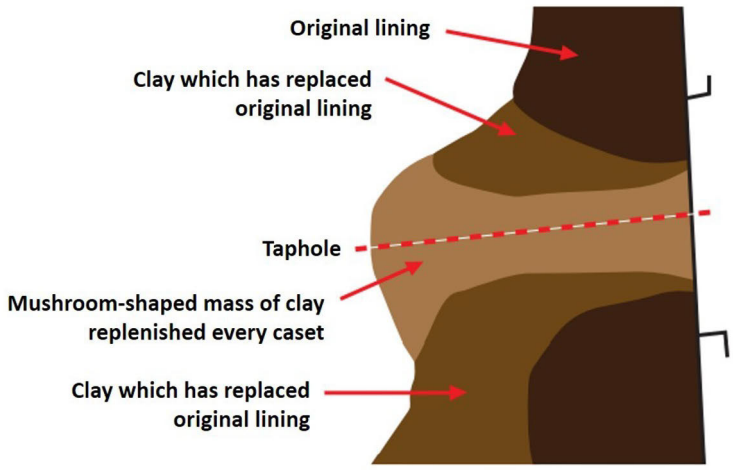

Figure 10. *Schematic of the mushroom formation from taphole clay (Cameron et al. 2020).*

According to the initial slag-iron interface (l-l interface) level, the tappings can be divided into three types: iron-first, simultaneous, and slag-first flow, which roughly indicates the l-l interface level at the start of the drainage to the furnace operator. The iron-first flow occurs if the slag-iron interface is above the taphole level at the start of the drainage. This tapping pattern begins with iron-only flow, but slag will start to flow out as the l-l interface reaches the taphole opening. Then, in general, a simultaneous flow of both liquids continues until gas escapes from the taphole, which leads to a termination of the tapping. During this process, the time between the start of the iron flow and the start of the slag flow is called slag delay. Conversely, a slag-first flow happens when the initial l-l interface is (far) below the taphole, which is more likely in a large furnace with multiple tapholes. The iron flow will not occur at the start of tapping if the pressure gradient induced by the slag flow is not sufficient to lift the iron. However, with only slag flowing out, the l-l interface (with a local upward bending near the taphole) raises gradually along with the iron accumulation in the hearth. After a time period (i.e., negative slag delay), the iron also starts to flow out when the l-l interface is high enough to establish a stable two-liquid flow. Therefore, the slag-first flow pattern also results in a simultaneous flow of both liquids until the end of the tap. The third flow pattern is characterized by a simultaneous flow of both liquid phases. This pattern occurs if the l-l interface locates at, or very close to, the taphole at the beginning of the drainage. The big pressure gradient in the slag phase can lift and drain iron from the level well below the taphole. Therefore, the final l-l level can be very low. This means that

both interfaces bend considerably toward the taphole at the end of the drainage (Figure 11).

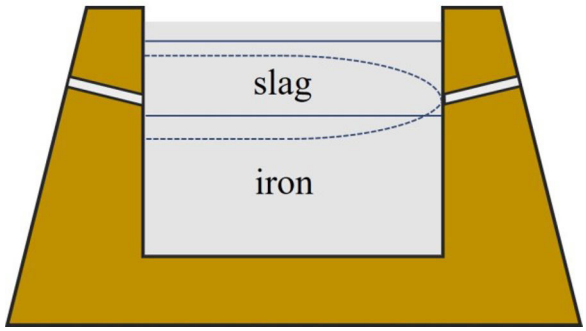

Figure 11. *Illustration of initial and final interface states at tapping. Liquid levels at the start (solid lines) and at the end of drainage (dashed lines).*

3. Studies on the blast furnace hearth phenomena

This chapter gives a brief description of some experimental and numerical works on BF hearth phenomena, particularly hearth drainage. It mainly focuses on the models and approaches closely associated with the work conducted in this thesis.

3.1. Hearth lining condition and hearth erosion

The furnace hearth, as the core part for the BF system, exerts considerable influence on the integrated performance of the BF and its lining state is closely related to the BF campaign life length. The furnace hearth is in an extremely hostile environment characterized by high temperature, high pressure, and flow of chemically aggressive molten iron and slag. Thus, it is almost inevitable that the hearth lining will suffer erosion during the campaign. It is necessary to stop the furnace operation for hearth maintenance, which leads to big production and economic losses. Therefore, a timely and well-planned lining repair is essential. Otherwise, the erosion may cause severe lining damage with the catastrophic outcome which may terminate the campaign in an unplanned fashion. Many researchers have studied hearth erosion based on different simplified models considering heat transfer and/or fluid flow. Such models give some guidance for the BF operators for the optimization of the lining protection and campaign life extension.

3.1.1. Erosion of hearth lining

There are many reasons for hearth lining erosion like the carburization of the hot metal, thermal stress and shear stress induced by liquids flow, exceptional water leakage, as well as chemical attack from alkali, zinc oxides, etc. (Cameron et al. 2020; Raipala, 2003; Vats and Dash, 2000). Severe lining erosion may cause an “elephant-foot-shaped” or a “bowl-shaped” lining profile which has been found at the hearth dissections of quenched furnaces (Inada et al. 2009; Gao et al. 2020; Jiao et al. 2016; Jiao et al. 2015). The “elephant-foot-shaped” erosion occurs mainly near the corner between the sidewall and bottom of the hearth. It usually arises in a hearth with a strong circumferential iron flow which is generated by a dead man with a bad permeability in the center or/and a partially floating dead man. The “bowl-shaped” erosion pattern is characterized by an intensive erosion in the center part of the bottom lining. This erosion pattern is more likely to occur for a hearth with a totally sitting dead man (of uniform permeability) or a totally floating dead man.

The “elephant-foot-shaped” lining erosion is more common and it is also more likely to cause hearth breakout compared to the “bowl-shaped” erosion. Therefore, it is essential to find solutions to prevent or control “elephant-foot-shaped” erosion. One solution is to suppress the

circumferential liquid flow in the hearth. A common way to restrain the circumferential flow is designing a hearth sump with enough depth to yield a dead man in a fully floating state (Liu et al, 2012). In addition, extending the taphole length is also helpful to suppress the peripheral flow since this drains liquids from the hearth center (Shao, 2013). The other solution for controlling hearth erosion is by generating stable self-protective skulls on the inner wall of the hearth to avoid a direct contact of the hot liquids and hearth lining. A protective layer can be formed by adding certain components (e.g., titanium) to the charged materials or by injection of such through the tuyeres to form a protective layer with a high melting point (Gao et al. 2020). Intensifying the cooling of the sidewall and bottom of the hearth can also yield a protective layer of iron or slag. However, overcooling may generate a too thick skull which decreases the hearth volume. Excessive bottom overcooling may also cause dead man inactivation because it solidifies the lower region of a sitting dead man (Raipala, 2003). Thus, a good strategy is necessary for controlling the skull layer thickness to a proper extent.

3.1.2. Hearth erosion models

To monitor the hearth state, a large number of thermocouples are installed inside the bottom and sidewall linings to measure the local temperature, which can be employed for real-time lining thickness estimation. Inverse heat conduction models are commonly applied to predict the erosion profile of the hearth based on temperature readings from thermocouples (Torrkulla and Saxén, 2000; Gonzalez and Goldschmit, 2006; Brännbacka and Saxén, 2008). The 1150 °C isotherm is usually taken as the boundary between molten iron and the solid material (i.e., buildup or lining materials) in the hearth, so the essence of the models is estimating the location of the 1150 °C isotherm. This type of model can indicate the hearth lining profile to help the BF operators understand the furnace state. However, it is not possible to get a very accurate estimate of the erosion profile since the model is affected by measurement errors of the thermocouples and also by differences between the real and assumed material properties, thermal contact between refractory blocks or bricks, etc. Furthermore, the model provides little explanation of the internal conditions that caused the estimated wear.

Some CFD models also have been established to further study hearth erosion considering only heat transfer, only liquid flow, or both. To study the effect of the shear stress caused by the liquid flow on the hearth erosion, some researchers (Vats and Dash, 2000; Dash et al. 2001, 2004; Shao and Saxén, 2012a) developed CFD models to examine the influence of various operating factors. The models only consider hot metal flow and

run in a steady state. Still, they can provide useful indications about flow-induced hearth erosion, especially for the lower part of the hearth where hot metal is the only liquid. Dash et al. (2001, 2004) investigated the effect of the taphole conditions (taphole length and angle) on the shear stress acting on the hearth sidewall. The main findings were that a longer taphole generally reduces the peak of the shear stress but the optimum taphole length is also related to the dead man floating state. An optimum taphole angle, 15^{o}, was determined for both floating and sitting dead man states. Shao and Saxén (2012a) studied the role of the dead man state on the hearth bottom erosion and found that a completely floating dead man yields a more uniform shear stress distribution on the hearth bottom, which can relieve the hearth bottom erosion to some extent. CFD models with conjugated the heat transfer and liquid flow in the furnace hearth have also been proposed (Shibata et al. 1990; Guo et al. 2008; Dong and Zulli, 2020; Lai et al. 2021). In this approach, the hearth is explicitly divided into a liquid zone (hot metal pool) and a solid zone (refractory linings). Although these models are more realistic and comprehensive, there are still some shortcomings for this type of models, e.g., that skull formation is seldom considered.

3.2. Laboratory-scale physical modelling studies of hearth drainage

Experimental studies of BF hearth drainage, as the base for drainage investigations, have been started in the 1970s. Early experimental work conducted by Fukutake and Okabe (1976) examined the slag flow during hearth drainage to clarify what resulted in the over-accumulation of the liquids in the hearth. For the experiments, the flow of an aqueous solution of glycerol in a three-dimensional packed bed model was applied to simulate the slag flow in the hearth. To quantify the experimental results in a generalized way, an important dimensionless variable characterizing the hearth tapping, a flow-out coefficient, was proposed. It was found that the flow-out coefficient is closely related to the residual slag ratio, i.e., the ratio of the residual slag amount at the end of the drainage and the initial slag amount in the hearth. Fukutake and Okabe assumed that the slag-iron interface stays horizontal and static at the taphole level as the slag flows out. Thus, they only designed the single-liquid (slag) flow experiments ignoring the molten iron phase flow and its effect on the slag tapping.

Later, this assumption was re-examined by conducting the two-liquid flow experiments in a two-dimensional tapping model, a H-S cell (Tanzil et al. 1984; Tanzil 1985). The H-S cell consists of two parallel and transparent plates with a small (around 1 mm) gap between plates, as shown in the upper panel of Figure 12 (Tanzil et al. 1984). It can be mathematically shown that the liquid flow in the H-S cell can mimic the flow in a three-

dimensional packed bed based on the viscous flow analog. Different bed permeabilities can be simulated by adjusting the gap between two plates. A natural advantage of the H-S cell is the good flow visualization that allows for observations of the interface behavior during the drainage. For the experiments, different mixtures of water and glycerol, as well as mercury were used as the analogues for the molten slag and iron, respectively. Experiments were conducted with different interface levels, slag viscosity, and flow rates. The experimental results indicated that it is possible to drain out hot metal from a level well below the taphole. They also showed that in general a simultaneous flow of the two liquids is dominant during the whole drainage period, which corrected the earlier findings of Fukutake and Okabe. During the simultaneous flow period, a substantial local pressure gradient is generated near the taphole in the more viscous phase and this induces a bending of the two interfaces towards the taphole. To compare the differences between the single-liquid and two-liquid flows in the H-S cell, single-liquid flow experiments were also undertaken and the experimental data were merged to describe the correlation between the flow-out coefficient and residual glycerol ratio. The results illustrated that the single-liquid experiments result in an underestimation of the residual ratio of the more viscous phase, especially for the case with a high outflow rate of it.

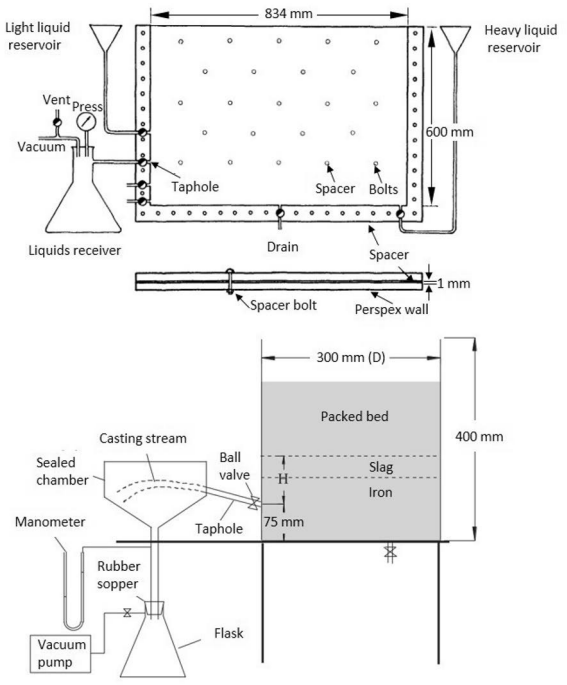

Figure 12. *Hele-Shaw cell (upper panel, Tanzil et al. 1984) and packed bed model (lower panel, He et al. 2012).*

Based on the findings of Tanzil et al. (1984), Zulli (1991) made more two-liquid flow experiments in the H-S cell and packed-bed model. To account for the effect of the iron flow, he corrected the expressions of the flow-out coefficient for both the flow in the H-S cell (Eq. (1)) and packed bed model (Eq. (2)). The modified flow-out coefficients are given as

$$F_{\mathrm{L}} = 180\frac{(1-\varepsilon)^2}{\varepsilon^3}\frac{1}{\phi^2 d_{\mathrm{P}}^2}\frac{\mu}{\rho}\frac{U_0}{g}\left(\frac{D}{H_{\text{l-g,0}} - H_{\text{th}}}\right)^{1.94} \tag{1}$$

$$F_{\mathrm{L}} = 180\frac{(1-\varepsilon)^2}{\varepsilon^3}\frac{1}{\phi^2 d_{\mathrm{P}}^2}\frac{\mu}{\rho}\frac{U_0}{g}\left(\frac{D_{\mathrm{h}}}{H_{\text{l-g,0}} - H_{\text{th}}}\right)^{1.4} \tag{2}$$

Where ε is the porosity of the bed, d_{p} is the particle diameter, ϕ is the sphericity of the particles, U_0 is the mean superficial velocity, μ and ρ are the viscosity and density of the more viscous phase, respectively, g is the gravitational acceleration, D is the width of the H-S cell, D_{h} is the diameter of the packed bed model, $H_{\text{l-g,0}}$ is the initial liquid-gas (l-g) interface level above the base of the model, and H_{th} is the taphole level. Bean (2008) further revised the flow-out coefficient expression to consider the variation of tapping rate, continuous production of liquid, and sump depth.

More drainage experiments have been done by He et al. (2006, 2009, 2012) to study the gas-liquid interface instability phenomenon, i.e., viscous fingering, during the drainage. The authors proposed the hypothesis that viscous fingering is the main root for unexpected premature discharge of the gas in the BF, which can strongly shorten the tapping time and also cause excessive taphole stream splashing. The experimental modelling studies were conducted by applying both the H-S cell (cf. the upper panel of Figure 12 (Tanzil et al. 1984)) and the packed bed model (cf. lower panel of Figure 12 (He et al. 2012)). During the experiments, mineral oil and 70% $ZnCl_2$ solution were employed to simulate molten slag and iron in the hearth (He et al. 2006, 2009, 2012). Using the H-S cell, the effect of the draining rate on the tapping time was studied (He et al. 2006, 2009). The upper panel of Figure 13 (He et al. 2009) shows how the gas break-through time decreases with the draining rate and that the tapping time becomes very short when viscous fingering occurs. Thus, the gas break-through time could act as an indicator for judging if the viscous fingering occurs for the cases with fixed initial liquid volumes. Depending on whether viscous fingering occurs, the drainage can be divided into three types and three relevant examples of the interface profiles at the end of tapping are illustrated in the lower panel of Figure 13 (He et al. 2009). It shows, for high draining rates, that some (one or many) air channels develop in of oil phase in the local region near

the taphole during the tapping, which is called viscous fingering. The packed bed model was also used to study the role of the permeability of uniform beds and the effect of the bed heterogeneity on the drainage time. This demonstrated that viscous fingering is more likely to appear for a bed with lower permeability or a heterogeneous bed.

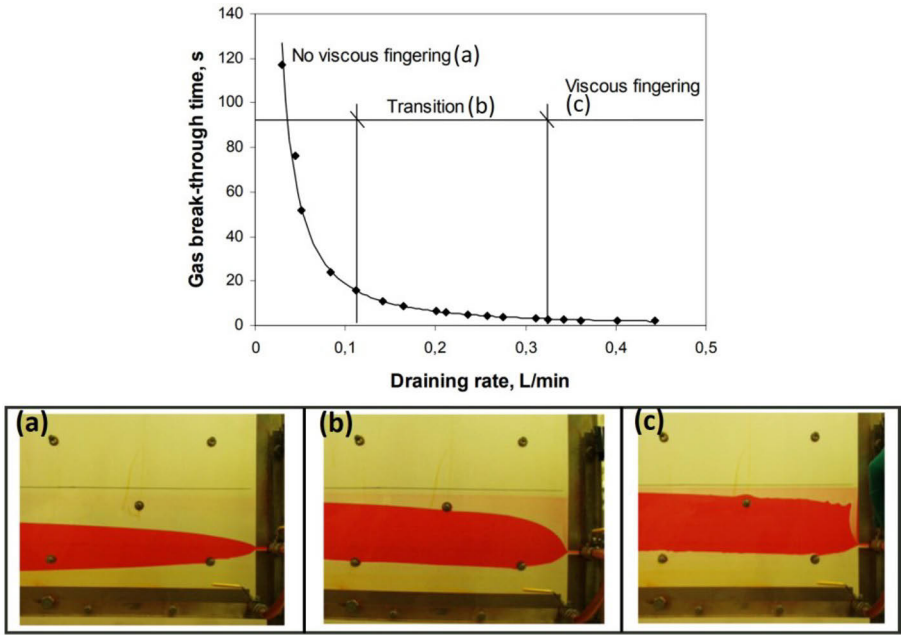

Figure 13. *Effect of draining rate on gas break-through time (upper panel) and interface profiles of three types of drainage at the end of tapping (lower panels) (He et al. 2009).*

To gain a deeper understanding on the viscous finger and early gas discharge during hearth drainage, He et al. (2012) undertook more experiments in the packed bed model to examine how the furnace operating conditions and a coke-free zone affected the gas break-through time. To apply the experimental results to the practical system, the results were presented in both the dimensional and dimensionless format. The main findings were that the gas break-through time decreased with the draining rate, slag viscosity, but increased with the initially accumulated liquids in the hearth. The existence of a coke-free zone increased the tapping time significantly if the zone extended into the slag phase. It should be noted that the same conclusions about the role of the coke-free zone on the hearth drainage were drawn by Zulli (1991).

Nouchi et al. (2003) designed a three-dimensional continuous drainage model to investigate the role of the coke-free space on the hearth drainage efficiency. A schematic of the experimental model is shown in Figure 14

(Nouchi et al. 2003). For the experiments, nitrogen, fluoride fluid, and liquid paraffin were employed as the substitutes for the blast gas, molten iron, and molten slag in the system. The vessel was first charged by plastic beads with 6 mm diameter and the size of the coke-free space was controlled by a net that could keep the bead bed on different levels. Both the fluoride fluid and liquid paraffin were supplied from the top surface of the model through a distributor to study a continuous tapping.

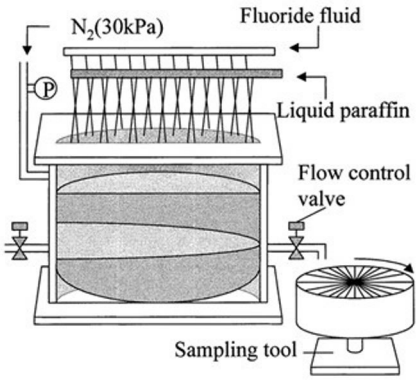

Figure 14. *Schematic of the continuous drainage model (Nouchi et al. 2003).*

Drainage experiments were conducted for both cases with and without a coke-free space. The results illustrated that the quantity of residual paraffin decreased greatly at the end of the drainage for the case with coke-free space shown in (a) and (b) of Figure 15 (Nouchi et al. 2003). It is mainly caused by the paraffin flows along the peripheral region, i.e., in the coke-free space, when the coke-free space exists, as seen in (c) and (d) of Figure 15, which decreased the paraffin flow resistance sufficiently and improved the drainage efficiency. Panels (e) and (f) of Figure 15 show for a bed with a coke-free space, that the fluoride outflow rate saturates quickly and that the paraffin outflow rate increases especially in the latter stage of drainage. The effect of an asymmetric coke-free space on the continuous drainage was also studied by a case with coke-free space only at the taphole one side (i.e., half of the coke-free space in (b) of Figure 15 was filled by particles). The investigators observed that the tap is longer when the liquids were drained through the taphole on the coke-free space side because the paraffin-gas interface level remained higher after tapping from the other side, i.e., through the packed bed. In addition, the longer tap time also makes the paraffin flow rate and volume ratio of paraffin to fluoride in the outflows higher.

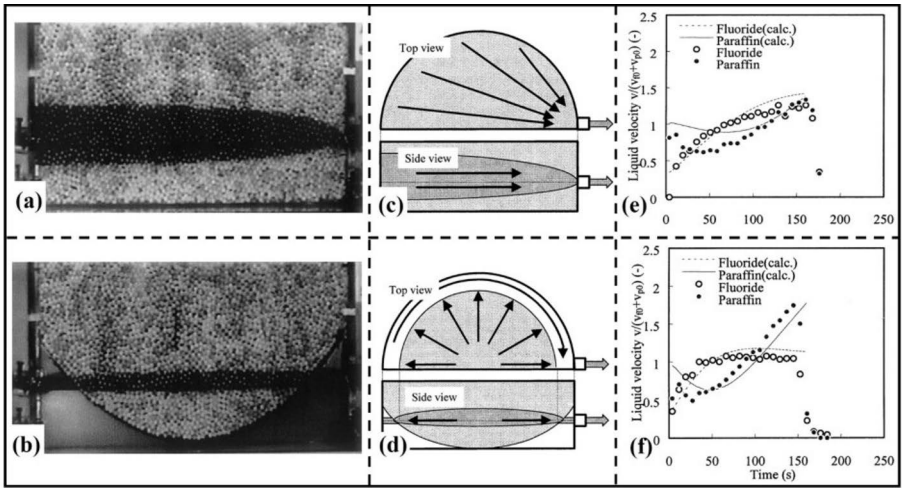

Figure 15. *Bed state, flow path of paraffin, and liquid outflow rates. (a) bed without coke-free space, (b) bed with coke-free space, (c) paraffin flow path without coke-free space, (d) paraffin flow path with coke-free space, (e) liquid flow rates evolution for the case without and (f) with coke-free zone (Nouchi et al. 2003).*

Except studying the integrated hearth tapping directly, some drainage experiments also have been finished to focus on other respects about the drainage. Luomala et al. (2001) built a three-dimensional packed-bed model with different bed conditions to investigate the hot metal flow path in the hearth during the drainage. Only water was fed into the model and a set of sensors was installed to help determine the flow path of water. The experimental results revealed that the existence of coke-free space shortens the hot metal residence time in the hearth during the drainage, but a center-blocked dead man leads to an opposite effect, which is the result of a different hot metal flow paths.

3.3. Numerical models of hearth drainage

The hearth of a running BF is an extremely harsh environment, so it is almost impossible to access the hearth and study its drainage directly by measurements. Cold experiment modelling, as one of the important tools, plays a key role to help researchers understand the basic mechanism of the hearth drainage. However, there are some limitations of the experimental methods, such as high economic and labor costs, especially for a large-scale experiment, difficulty in information extraction, etc.

Considering these limitations, many mathematical models have been developed to study the drainage further.

3.3.1. Online models

For the BF operator, a real-time detection and prediction of the liquid levels inside the hearth are necessary, because bad drainage may cause an excessive liquids accumulation in the hearth, thereby further disturbing the normal running of the whole furnace (Brännbacka, 2004). Real-time liquid-level information could guide furnace operators to adjust operation strategies in time, if necessary. In order to predict the hearth liquid levels for a running furnace, some online models have been established mainly based on mass balances or measured electromotive force (EMF) between sets of electrodes installed in the lining or on the hearth shell.

The EMF is an interesting signal related to the liquid levels in the hearth, but it often exhibits serious noise and drift, which is probably partly caused by other process variables, such as the thermal state and hearth pressure. Thus, using the EMF signal directly to predict the liquid levels is not feasible. The EMF is still a simple, continuous and practical variable reflecting the hearth liquid level. Filtering can be used to address the signal drift and noise problem to some extent. Some promising applications of EMF have been reported for hearth liquid level estimation in real time (Alter et al. 2013; Hattink et al. 2011). Advanced EMF-based prediction models have also been established by integrating the EMF signal with methodologies such as time series models and neural networks (Gomes et al. 2011, 2017). These authors reported a successful application predicting the hearth liquid level in a BF in Brazil for up to 30 minutes (Gomes et al. 2011). Later, Gomes et al. (2017) developed a more accurate model, i.e., a time-delay neural network model and this model presented better performance as well as longer forecasting time (up to one hour ahead). The liquid level information one hour ahead could guide and help the furnace operators to control and optimize the furnace operation. Despite the reported success and the straightforward use of such models for online applications, the approach also suffers from several drawbacks: since the true liquid levels are unknown, the quality of the predictions cannot be assessed. Further, a purely data-driven technique does not (necessarily) yield liquid-level estimates that obey the material balance equations. Yet another is the difficulty to predicting the slag and iron level separately, as there is still not even a consensus on whether the EMF signal reflects the iron level, the slag level, or a combination of both.

Another common method for liquid-level prediction in the hearth is to use the mass balance equations based on the inflows and outflows of the iron and slag. To realize online liquid-level tracking, the production and

drainage rates of the liquids should be measured or calculated in real time. The production rate of the molten iron can be calculated using an oxygen balance based on the top gas and blast gas components as well as the oxide content in the iron-bearing materials. Assuming a fixed slag ratio, then the slag production rate is also obtained. The iron outflow rate is often predicted by measuring the hot metal level change in the ladle/torpedo monitored by radar or through direct weighing. The slag outflow rate, in turn, is usually estimated by measuring the heat transfer to the cooling water in the granulation unit or by weighing the granulated slag. The balances give estimates of the accumulated liquid volumes in the hearth, and using this the iron and slag levels can be estimated if the dead man state (i.e., porosity and floating state) and hearth profile are known. This gives a possibility to track the short-term changes of the liquid levels. Like other online liquid level estimation models, the mass balance-based model also shows drifting estimates due to noise and errors in the process data. Therefore, proper data processing and filtering strategies are essential to correct the estimated levels. Such mass balance models have been developed based on the assumption that the dead man fills the hearth and that the hearth profile is fixed (Brännbacka and Saxén, 2001; Agrawal et al. 2016; Nightingale et al. 2001). Correction factors of the tapping rates of slag and iron or more sophisticated filters (such as a Kalman filter) were introduced to achieve more feasible estimates. Based on the basic model, Brännbacka and Saxén (2004) developed a more advanced model, which considers both the time-varying hearth profile (due to lining wear) and dead man floating state. Later, Roche et al. (2019) applied the mass balance-based online model to a multi-pool system to estimate the liquid levels of a hearth with three tapholes. The multi-pool design divides the hearth into two or more regions, which makes it is possible to consider local level differences induced by the tapping from alternating tapholes in a large BF.

3.3.2. Offline models

The offline hearth drainage models mainly include two categories, i.e., mathematical models expressing simplified fluid mechanics relations and the more detailed partial differential equation-based computational fluid dynamics (CFD) models. The latter also includes sophisticated models integrating CFD with the discrete element method, i.e., CFD-DEM. The general advantages of the first category models are faster computation speed and higher flexibility for adjustment. However, there are also many merits of the CFD-based models, e.g., rigorous treatment of the mass, momentum, and energy balance equations, more comprehensive and detailed results as well as better visualization facilities. Both types of models have been successfully applied to study the effect of different factors on the drainage.

Nouchi et al. (2005) developed a simplified mathematical model to study the role of process parameters (like hot metal production rate, coke diameter, slag viscosity, etc.) and tapping strategies on the amount of residual liquids in the hearth. The main findings were that hearth permeability has a more significant effect on the residual slag amount than slag viscosity, and that applying a drill rod with a big diameter and high-quality taphole clay can lower the maximum slag level. Brännbacka and Saxén. (2003) applied a simple mass balance based model, assuming constant inflow and outflow rates of hot metal and slag, to study the effect of production, dead man state, hearth diameter, plugged time, etc. on the liquid levels and slag delay for a one-taphole BF. The model was extended by Shao and Saxén (2012b) to include time-dependent tap rates by considering the complex two-phase flow conditions in the taphole. The model was used to simulate slag delays over 20 days of a practical BF for model validation: the results were compared with the industrial measurements showing that the model could track the changes of slag delay.

Also considering the effect of the taphole on the drainage, Iida et al. (2008) established a tapping model which considers the pressure drop of the liquids in the coke bed (at the entrance of the taphole) and in the taphole channel. In addition, the model included the influence of the coke consumption in front of the taphole caused by the carburization of hot metal and oxidation by slag, and the gradual enlargement of the taphole entrance due to wear. As a numerical simplification, Iida et al. (2008) assumed that the hot metal and slag are flowing through the taphole as a mixture, treating them as one liquid phase. However, Shao and Saxén (2011) pointed out that this assumption is somewhat controversial, as the big density difference of the phases would be conductive to form a stratified flow in the taphole. Based on this, a hearth drainage model coupled with a two-fluid model of the taphole flow was proposed by Shao and Saxén (2011), assuming that the two liquids are fully stratified in taphole. The model was used to investigate the evolution of liquid levels and flow rates. The simulation results demonstrated that the internal conditions of the furnace (like coke diameter and coke bed porosity) have a significant influence on the residual amount of slag and iron.

To consider the role of a dead man with locally low permeability on the hearth drainage, Iida et al. (2009) introduced the concept of a vertical low-permeability zone in their previous model (Iida et al. 2008) for developing an integrated model to describe asymmetric drainage behavior. The vertical low-permeability zone divides the hearth vertically into two sections, making it is possible to investigate the differences that arise when two alternating tapholes are operated. To examine the validity of the model, the results were compared with the observed data from a

reference BF, showing a reasonable agreement with respect to the imbalance in the quantities of slag drained for the two tapholes. Saxén (2015) used a similar two-pool model as Iida et al., but also considered a possible dead man floating. Instead of not permitting slag cross-flow between the pools (as in the model of Iida et al.), the flows of metal and slag between the pools were managed by the cross-flow coefficients. The model was finally evaluated by examining the effect of the size of the two pools, the dead man floating state, and the existence of the impermeable zone on the liquid levels and slag delay. Based on the model established by Saxén (2015), Roche et al. (2018) developed a two-pool tapping model with dynamically varying pool-size distribution during the drainage, so the tapping pool may expand as the other pool shrinks along with the drainage. Compared with the case with fixed pools, the drainage duration is longer and the slag delay is shorter for the case with dynamic pools. The model was also employed to simulate the drainage behavior of a reference BF and the results showed that the model can reproduce some key tapping variables. Roche et al. (2020) later established a comprehensive mathematical model to simulate the alternate drainage of a (large) BF with multi tapholes. This model considered the pressure losses in three parts, i.e., the dead man, taphole entrance, and taphole. This model was applied to predict the outflow rates and liquid levels for different cases, and it was demonstrated that observed outflow patterns in an industrial BF (BF7 of Tata Steel Europe) could be reproduced, both for quasi-stationary and dynamic states. This model was able to explain the reason behind the complex evolution of the outflow of the slag phase, which strongly resembled the experimental results concerning the outflow of paraffin in the study by Nouchi et al. (2003) (cf. Figure 15 (e) and (f)).

Some CFD-based drainage models have also been developed for gaining more comprehensive information about the conditions during the drainage process. The volume of fluid (VOF) method has mainly been applied for tracking the interfaces between impermeable fluids, so it is suitable to describe the slag-gas and slag-iron interfaces in CFD-based hearth drainage models. Nishioka et al. (2005a, 2005b) developed a three-dimensional VOF-based CFD model which was validated by industrial data. The model was applied to investigate the effect of hearth operation conditions (such as coke size, slag viscosity, etc.) on the evolution of the average slag thickness, interface levels, and drainage rates during the tapping. The main findings were that coke size and dead man voidage have a clear effect on the maximum gas-slag interface height and that an increased coke size or dead man voidage is an effective way to limit the maximum gas-slag interface level. Ashrafian et al. (2006) investigated the role of the material properties (i.e., density and viscosity) and bed permeability in large ranges on the flow rates and slag delay by a two-

dimensional VOF-based drainage model. Studying the free slag-gas interface behavior near the hearth taphole, Yoon and Park (2021) established a two-phase 3D drainage model, which demonstrated that viscous fingering may occur when the liquid-gas interface was near the outlet. This was identified by visualization of the liquid-gas interface shape during the simulation. Shao and Saxén (2013a) studied the transient iron- and slag-flow behavior in the taphole by a three-dimensional VOF-based tapping model. The simulation results illustrated that both dispersed and separated flow patterns could appear in the taphole at different stages of the tapping and that gravity plays a key role for the flow pattern.

The VOF-based method is attractive due to its simple numerical expressions, but a high grid resolution is necessary for accurate interface tracking, causing high calculation costs. In addition, the interfacial force is not considered in the VOF method, which affects the simulation accuracy to some extent. To include the interfacial force in the drainage model, Shao and Saxén (2013b) proposed an improved two-fluid (TF) model to describe iron and slag drainage in the hearth. The model was compared with the VOF model both for the iron-slag and water-oil systems and it was found that the improved TF model provides a more accurate prediction of single drainage rates and slag-iron interface angle. To reduce the computational load, Kaymak et al. (2017) developed a single slag phase flow model with two moving interfaces to simulate the tilting of both interfaces during the hearth drainage process. For this model, the moving interfaces were modeled by the moving mesh physics in Comsol.

To consider the effect of the dynamic dead man and the corresponding coke-free zone on the hearth tapping, some CFD-DEM models have been proposed to reproduce more realistic drainage conditions. Bambauer et al. (2018) developed a transient CFD-DEM overall model, where the gas, liquid, and solid flow in a down-scaled BF were considered. It illustrated the interaction between the liquid levels and the dead man floating state in the hearth. To reduce the computation load of the CFD-DEM method, Vångö et al. (2018) established an unresolved CFD-DEM model which considered the dynamic behavior of the particle bed, but neglected the flow around each particle. The model was verified firstly by a drainage experiment, and then applied to simulate the iron and slag tapping in a small-scale BF hearth.

3.4. Conclusions

The hearth tapping has been studied by two- and three-dimensional physical models, where the model settings are analogous to the practical system. Even though the experimental models are simplified to make it feasible to conduct the experiments, tests in them still supply interesting

information that can be used to gain knowledge of the behavior of the industrial system and for the development of simulation models. In addition, quantitative analysis on the drainage experiments supports verification of the numerical models. To gain more detailed process information, hearth drainage and the associated hearth erosion state have been simulated and predicted by different numerical models based on experimental and industrial data. Some online models have also been established and applied to the real system to guide BF operators to optimize the furnace operation.

Since the hearth environment is hostile, it is very difficult to gain information about the conditions in the hearth by direct measurements. Lack of information also makes it difficult to formulate and verify numerical models. Gaining additional and more accurate information from physical experiments could help to solve the above-mentioned issue to some extent. This is a motivation for the work carried out in this thesis, which will be summarized in the next chapter.

4. Main work in this thesis

This chapter briefly summarizes the main work done in this thesis, including an introduction of the methods applied, the main assumptions made, key findings, and a brief explanation of the results. This chapter is divided into five sections. Section 4.1 introduces an image analysis-based algorithm for automatic information extraction from drainage experiments and the details of the tapping experiments. Section 4.2 illustrates the application of the algorithm to detect the interface behavior during the drainage. Section 4.3 presents the application of it to quantitative analysis of the tapping experiments, and Section 4.4 outlines a numerical model of the H-S cell and some results of it. The final section describes an asymptotic hearth erosion model considering the flow field of hot metal in the hearth, the refractory lining, and the possible skull.

4.1. Drainage experiments and information processing by automatic image analysis (Papers I and II)

The traditional approaches to deal with the experimental hearth drainage data are limited to observing variables like tapping time and average outflow flow rates, but detailed information on, e.g., the evolution of the interfaces and flow rates, cannot be easily obtained. The outflow rates could be estimated by sampling, but it requires special and quite complex procedures (e.g., a carousel sampler used by Nouchi et al. 2003). To extract more detailed information from the drainage experiments, a more efficient approach based on a digital image analysis algorithm is developed and employed to analyze the results of hearth draining experiments in an H-S cell.

4.1.1. Experimental apparatus arrangement and procedure

A schematic of the experimental set-up is shown in Figure 16, including two main subsystems, the tapping experiment system, and the image recording system. The former includes the H-S model, a liquid receiver, a vacuum pump, an oil and water reservoir, and a lifting table. The image recording system is also a critical component because high-quality images are prerequisites for employing image analyses to extract information from the experiments.

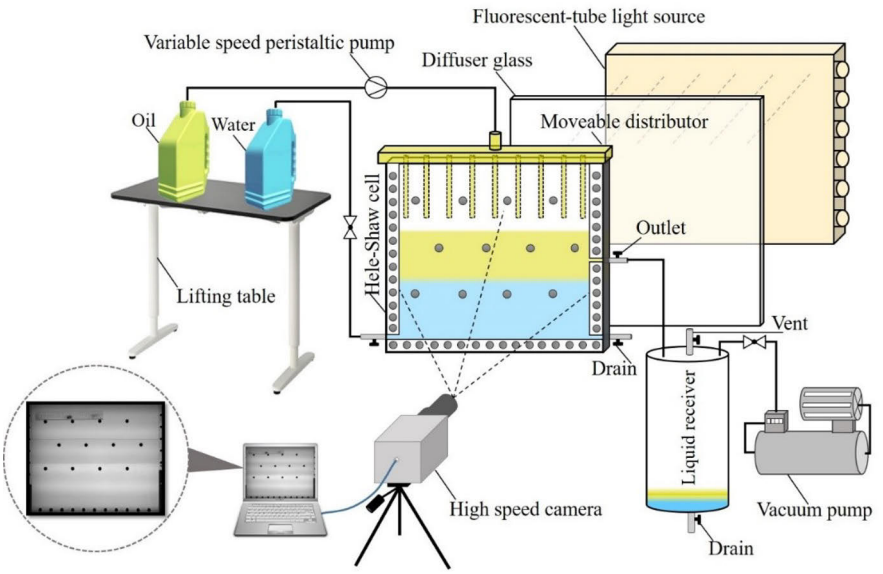

Figure 16. *Schematic illustration of the set–up of the drainage experiments.*

Water and engine oil were used in the H-S model to mimic the slag-iron flow in the BF system. The physical properties of the above fluids are reported in Table 1. The temperatures of the liquids were fixed (at 21 °C) in the experiments, to keep the viscosities and densities of the liquids constant. The core part of the system is the H-S model which is based on the flow analogue between the viscous liquid flow between two closely parallel plates and the flow in a packed bed (Tanzil et al. 1984). Flow visualization is realized by employing an H-S model instead of a three-dimensional packed bed.

Table 1. *Physical properties of fluids in the blast furnace (BF) and model system.*

Properties	System	
	BF: 1:iron, 2:slag	Model: 1:water, 2:oil
Density of phase 1, $\rho_{l,1}$ (kg·m^{-3})	6800	998
Dynamic viscosity of phase 1, $\mu_{l,1}$ (Pa·s)	0.0068	0.001
Density of phase 2, $\rho_{l,2}$ (kg·m^{-3})	2800	855 (876)
Dynamic viscosity of phase 2, $\mu_{l,2}$ (Pa·s)	0.43	0.131 (0.254)

According to the flow analogue, a Darcy flow in the packed bed model with hydraulic conductivity, K, can be characterized by the H-S model (explained in detail in Tanzil et al. (1984)), if

$$K = \frac{\rho_{\mathrm{L}} g b^2}{12 \mu_{\mathrm{L}}} \tag{3}$$

where b is the spacing between the plates in the H–S model, g is the gravitational acceleration, μ_{L} is the liquid viscosity, and ρ_{L} is the liquid density.

The definition of hydraulic conductivity in the packed bed model is

$$K = \frac{k \rho g}{\mu} \tag{4}$$

where k is the absolute permeability in the packed bed. Combining the above two equations yields

$$\left(\frac{k \rho g}{\mu} \right)_{\mathrm{Packed-bed}} = \left(\frac{\rho g b^2}{12 \mu} \right)_{\mathrm{H-S}} \tag{5}$$

In the experiments, water and oil flow through the H-S model emulate the flow of iron and slag in the furnace hearth, so

$$\frac{k \rho_{\mathrm{iron}} g}{\mu_{\mathrm{iron}}} = \frac{\rho_{\mathrm{water}} g b^2}{12 \mu_{\mathrm{water}}} \tag{6}$$

$$\frac{k \rho_{\mathrm{slag}} g}{\mu_{\mathrm{slag}}} = \frac{\rho_{\mathrm{oil}} g b^2}{12 \mu_{\mathrm{oil}}} \tag{7}$$

Since the fluids in the furnace hearth and those used in the experiments show practically equal density-to-viscosity ratios, the relation between the plate spacing (b) and the absolute permeability (k) of the packed bed is

$$b = \sqrt{12k} \tag{8}$$

Thus, by adjusting the gap between the two plates of the H–S model, it is possible to simulate the fluid flow in a packed bed with wide permeability ranges. In the BF hearth, a common effective coke particle diameter is 35 mm, and bed porosities in the range 0.30–0.40 have been reported. According to the empirical correlation between effective particle diameter and absolute permeability (Bear, 1972), a rough estimate of the

absolute permeability is, therefore, $k \approx 3 \times 10^{-7}$ m^2. Thus, by selecting $b =$ 2 mm, the H-S model can simulate the absolute permeability of the BF hearth coke bed.

The experimental procedure includes the following main steps:

(1) The lifting table was elevated to a certain level, followed by opening the ball valve to charge water into the model until the predetermined level was reached.

(2) The moveable oil distributor was fixed on top of the model and the peristaltic pump was started at low pumping speed to feed oil into the model slowly to create an oil layer with uniform and desired thickness.

(3) A settling time of a few minutes was allowed for both l–g and l–l interfaces to become absolutely stable. After this, the oil distributor was removed from the top of the model.

(4) The vacuum pump was switched on until the desired under-pressure was obtained in the receiver.

(5) The high-speed camera was turned on to record the drainage process.

(6) The outlet was opened fully. When air started blowing out through the outlet, the outlet was closed and the camera was switched off.

(7) The vent was opened to recover the receiver pressure, and the drain of the receiver was opened to empty the receiver.

4.1.2. Automatic image analysis algorithm

The proposed image analysis algorithm in Paper I is based on an accurate extraction of both l-g and l-l interfaces. After extracting the two interface profiles, more drainage process parameters, such as the interface levels, liquid volumes, and flow rates could be calculated. In addition, the bending points on the extracted interfaces can be determined for the calculation of the interface angles and bend ratios to characterize the interface bending. Figure 17a outlines the basic steps of the proposed image analysis algorithm, including three major modules: image pre-processing, interface extracting, and bending-point detection. A graphical illustration of the steps is presented in Figure 17b. The detailed algorithm is given in Section 3 of Paper I.

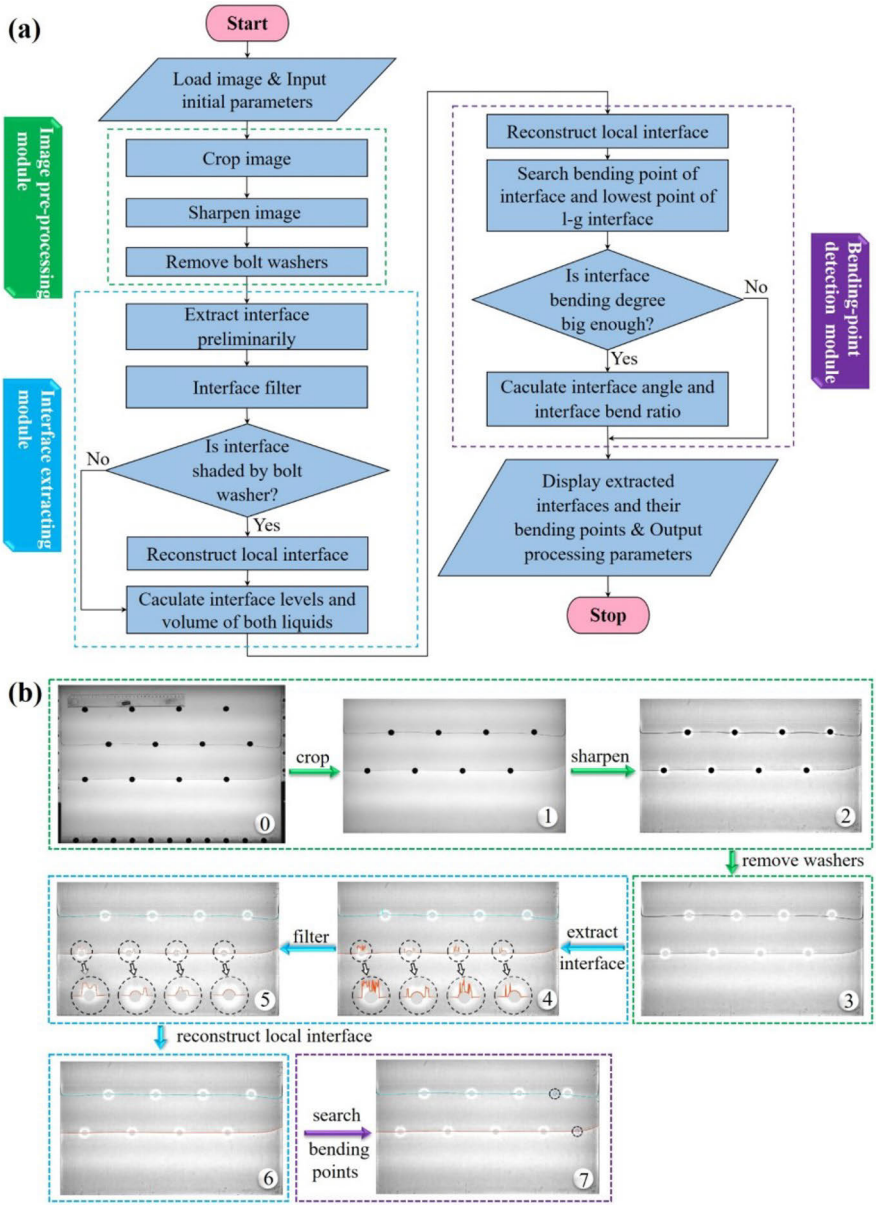

Figure 17. *Basic flowchart of the image analysis algorithm (a) and graphical illustration of the main steps of the image processing (b).*

4.1.3. Application of the algorithm

The basic and most important application of this algorithm is tracking both (l-g and l-l) interfaces to determine the interface level evolution. The

evolution of the two interface profiles during a tapping experiment is illustrated in Figure 18, which shows how the interfaces are descending and bending as the drainage progresses.

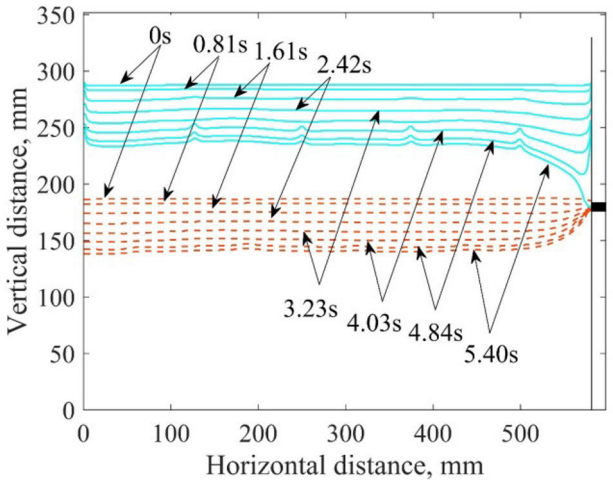

Figure 18. *Evolution of interface profiles in the drainage example.*

To quantify the evolution, the average level of the whole interface, and its horizontal part as well as bending part are calculated. The results, illustrated by an example in Figure 19a, illustrate that the bending part of the l-g interface descends more rapidly than the horizontal part, which is natural and partly due to a growing slope and partly to the gradual shifting of the bending point to the left. The l-l interface, in turn, shows an opposite result, where the horizontal part exhibits a higher descending speed since the right side of the bending part always extends to the outlet after oil starts to flow out. In addition, for both interfaces, the length ratio of the bending part to the full interface stays relatively low during the first part of the draining, but as the tapping progresses the ratio grows, so its effect on the overall interface level is also emphasized.

As the interfaces are known, and the spacing between the parallel plates in the H-S model is fixed, the volume of the liquids can easily be determined by integration. Figure 19b shows how the liquid volumes in the cell evolve. The results indicate that water is dominant in the outflow. It also indicates that the oil volume shows a considerably smaller decrease with time, even though the oil is in the upper layer. The main reason for this is the viscosity difference between oil and water.

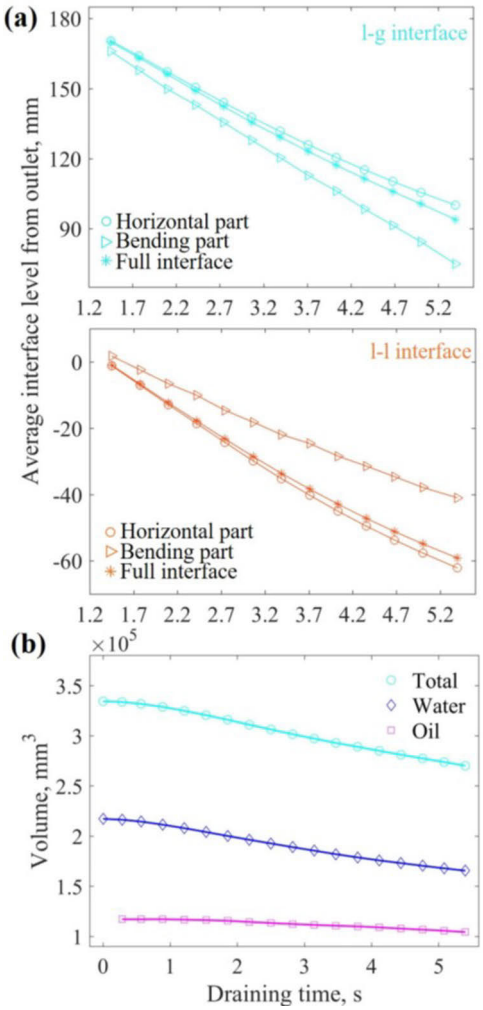

Figure 19. *Evolution of average interface levels (a) and liquid volumes (b).*

More interesting matters could also be extracted from the experimental results based on the tracked interfaces, such as the outflow rates and oil ratio in the outflow. Figure 20a shows how the water outflow rate raises at the beginning of drainage until arrives at a maximum, after which it decreases until the termination of the drainage. By contrast, the oil outflow rate increases gradually throughout the whole tapping process. Because the tapping time, which is one of the most important drainage indices, strongly depends on the local bending of the l-g interface, it is meaningful to quantify the interface bending by the interface angle for the drainage experiments. Thus, the interface angle and bend ratio of the bending part to the full interface are finally studied for the draining example. Figure 20b depicts the evolution of the two process variables

during the drainage, showing that both angles (upper panel of b) increase. However, the rates of increase are different: the l-g interface shows a slow initial but a rapid final increase, while the l-l interface has an opposite trend. As the oil descends, its surface starts bending considerably only when the draining process is near its end. The l-l interface, in turn, must bend immediately when the overall interface passes the taphole on its descent. For the l-l interface, the rate of increase of the angle levels out as the interface descends more deeply below the outlet since it becomes increasingly difficult to extract water from the system due to gravity. The more local bending of the l-l interface (cf. Figure 18) makes the angle larger than that of the l-g interface for most of the draining period, which is also indicated in the bottom panel of Figure 20b.

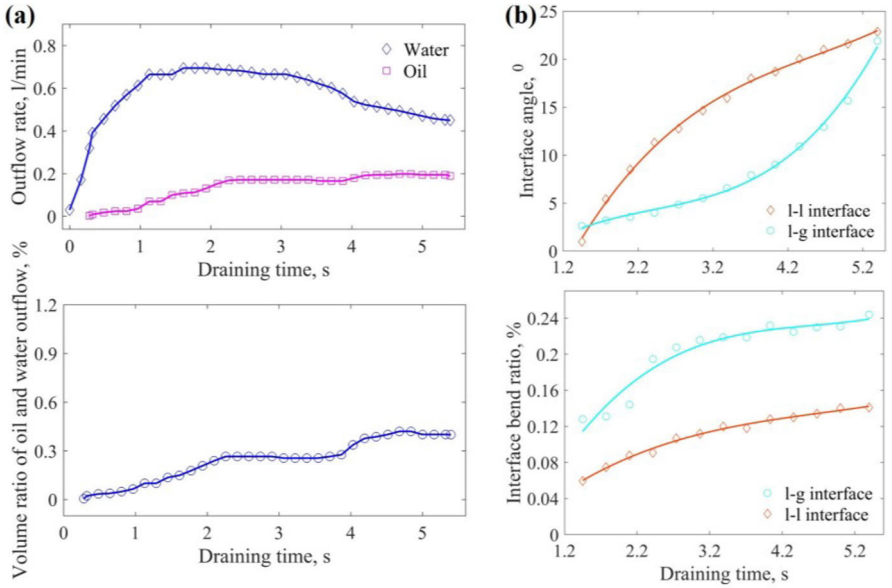

Figure 20. *Evolution of the volume outflow rates of water and oil and the ratio of oil to water in the outflow (subfigure a) as well as the interface angle and interface bend ratio evolutions for the draining example (subfigure b).*

4.1.4. Key findings

An image analysis-based method developed to automatically extract information and to calculate the key parameters (e.g., interface levels, liquid volumes, and interface angles) based on images recorded from two-phase draining experiments in the H-S slot model was successfully implemented. The approach can track and record the phase interfaces accurately during the draining, and based on this, more detailed information can be extracted to facilitate a quantitative analysis of the

drainage. The method can be applied to compile information from a large set of experiments for gaining a deeper understanding of the complex two-phase flow in the BF hearth and quantifying the findings for validation of numerical models.

4.2. Study of interface behavior during hearth drainage (Paper II)

The smooth tapping of iron and slag accumulated in the hearth is a prerequisite for a stable and efficient BF operation. Thus, it is essential to understand the drainage phenomena and the corresponding evolution of the liquid levels in the hearth. To investigate the l-l and l-g interfaces experimentally, a series of experiments were conducted in the two-dimensional H-S model to clarify the effect of some operation parameters on the draining behavior. In addition, the conditions under which the l-l interface at the end of tapping was close to the taphole or not below it were also studied. The whole draining process was recorded by a high-speed camera, and the pictures taken were interpreted by the automatic image analysis program (cf. section 4.1) to track both the l-l and l-g interfaces accurately during the drainage.

4.2.1. Experimental conditions and analytical methods

For the practical BF, before the beginning of tapping, the blast pressure, slag viscosity, as well as l-g and l-l interface levels may change from tap to tap, and all of these affect the hearth drainage. To study the above conditions, some tapping experiments were conducted according to Table 2, which varied four conditions, i.e., pressure difference (ΔP), initial l-l interface level ($h_{\text{l-l},0}$), oil viscosity, and initial oil layer thickness ($h_{\text{oil},0}$). The pressure difference is the difference between atmospheric pressure (that acts on the l-g interface) and the pressure inside the receiver. The $h_{\text{l-l},0}$ is expressed relative to the level of the outlet. The reported $h_{\text{oil},0}$ value is the absolute oil layer thickness in the model.

Table 2. *Experimental conditions. Changed parameters are written in bold. The dynamic viscosity of water is 0.001 Pa·s for all the experiments.*

Experimental group number	ΔP (bar)	Initial l-l interface level (mm)	Oil viscosity (Pa·s)	Initial oil layer thickness (mm)
1	0.3	10	0.131	20–100
2	**0.2**	10	0.131	–
3	**0.4**	10	0.131	–
4	0.3	**5**	0.131	–
5	0.3	**20**	0.131	–
6	0.3	10	**0.254**	–

To apply the experimental results to a real BF system, part of the results were dealt with in dimensionless format, i.e., as a residual oil (or water) ratio (α), dimensionless gas breakthrough time (τ), and flow-out coefficient (F_L), where the last factor is an important dimensionless variable characterizing hearth drainage. The definitions of the above parameters are

$$\alpha = \frac{V_{\text{end}}}{V_{\text{start}}} \tag{9}$$

$$\tau = \frac{t}{t_{\text{ave}}} = \frac{Qt}{Db\left(h_{\text{oil},0} + h_{\text{l-l},0}\right)} \tag{10}$$

$$F_L = \left\{180\frac{(1-\varepsilon)^2}{\varepsilon^3}\cdot\frac{1}{\phi^2 d^2}\cdot\frac{\mu}{\rho g}\right\}U_0\left[\frac{D}{H}\right]^{1.94} = \frac{\mu}{k\rho g}\cdot U_0\cdot\left[\frac{D}{H}\right]^{1.94} \tag{11}$$

where V_{start} and V_{end} are the total oil or water volume at the start and end of drainage, respectively. In the equations, D is the width of the H-S model, t is the gas breakthrough time, and t_{ave} is the time taken to drain the whole liquids above the outlet at the average tapping rate (Q), $h_{\text{l-l},0}$ is the initial level of the l-l interface above the outlet, $h_{\text{oil},0}$ is the initial absolute oil layer thickness in the model. Furthermore, ϕ is the shape factor of coke particles, ε is the bed porosity, d is the particle diameter, μ is the viscosity and ρ is the density of oil, U_0 is the superficial velocity, k is the absolute permeability of the coke bed in the hearth, and H is the initial level of l-g interface above the outlet.

4.2.2. Key findings and analysis

In the BF, when a tap starts, the initial amount of slag is related to the iron ore grade, coke quality, and the injection rate of pulverized coal, so it may vary with the quality and quantity of raw materials used. As for the initial l-l interface level (relative to the taphole level), it depends on the amount of accumulated iron in the hearth at the start of drainage, the dead man porosity, the taphole level, and the taphole length. Thus, it is possible to manage the initial l-l interface level to some extent by adjusting the taphole angle and taphole length. The blast pressure of an operating BF is usually relatively stable, so the difference between the internal pressure and the atmospheric pressure is often constant, but it may still change with the blast volume and BF top pressure. The slag viscosity is primarily related to temperature and its composition, but also the contents and characteristics of possible solid components (e.g., char) in the slag. As the temperature varies with the dynamic thermal state in the hearth, the slag

composition may also vary, which induces changes in the slag viscosity. The effect of all the above-mentioned variables on the residual liquid ratios, tapping time, and tapping end state have been studied in Paper II. Some of the results are shown in the following section.

Influence on residual ratio, tapping time

For the BF operation, the residual ratio of both liquids and draining time are essential parameters. Under certain conditions, a longer tapping time may correspond to a higher operation efficiency and lower economic costs. Since an extended tap duration causes lower residual liquid ratios and fewer taps per day and associated drilling and plugging of the taphole, the costs of refractory materials and taphole clay decrease.

Some experiments were conducted to study how the initial l-l interface level and pressure difference affect the residual liquid ratios and tapping time. Figure 21a depicts how the gas breakthrough time increased with the initial level of the l-l interface at a fixed initial oil-layer thickness. This is a natural consequence of the higher initial water level, as it delays the moment when oil starts flowing out. The lower panel of the figure shows that both the residual water and oil ratios decreased as the initial l-l interface rose. The residual water ratio decreased mainly because of an increased initial water volume. The latter is caused by the slightly longer oil tapping time at an increased initial l-l level and therefore lowers the residual amount of oil.

The effect of the pressure difference on the draining time is reported in the upper panel of Figure 21b, which demonstrates that the tapping time shortened dramatically with the pressure difference. The obvious reason is that the outflow rates of both liquids increased with the pressure difference. The decrease of the tapping time was more significant for a thicker initial oil layer. When the initial oil layer was thin, water was dominant in the outflow. However, along with the increase in the initial oil-layer thickness, the share of water to oil in the outflow decreased, particularly in the latter stages of the tapping. When the initial oil layer was thicker, the tapping time increased significantly due to the overall higher liquid level. The lower panel of Figure 21b depicts that both residual liquid ratios increase with the pressure difference increase (at a fixed initial amount of water and oil). This was presumably attributed to the fact that a higher pressure proportionally increases the draining rate of oil more than that of water, implying an earlier draining end. Thus, a lower pressure difference was beneficial for extending the tapping and emptying the hearth. However, in the BF system, a certain blast pressure is necessary to maintain normal operation conditions, e.g., to limit the gas velocity to prevent fluidization or flooding. The effect of other factors is illustrated in Section 3.1 of Paper II.

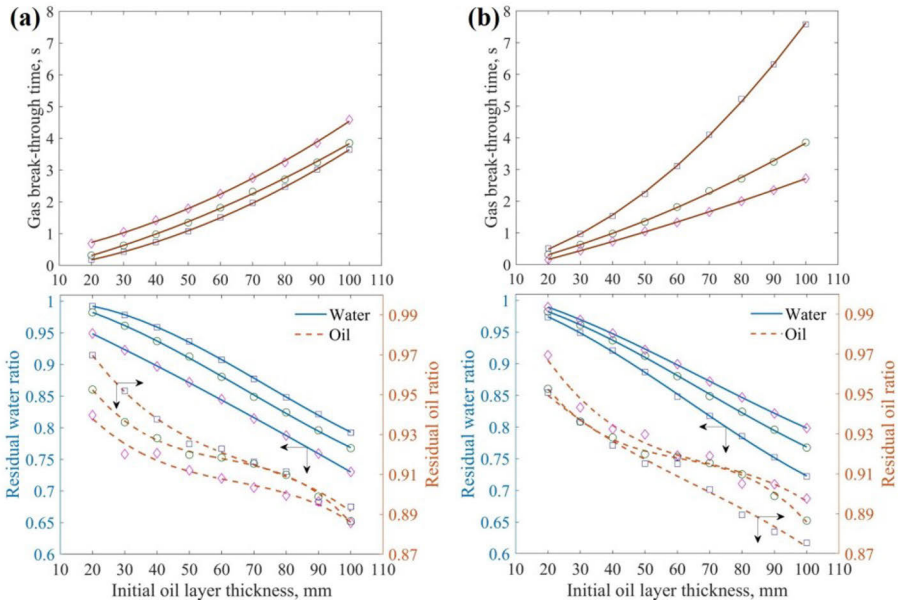

Figure 21. *Effect of initial oil-layer thickness on gas breakthrough time (upper panels) and residual liquid ratios (lower panels) at different initial l-l interface levels (a) and pressure difference (b). Conditions: (a) Pressure difference Δp = 0.3 bar, oil viscosity μ_{oil} = 0.131 Pa·s, initial l-l interface level $h_{l\text{-}l,0}$ = 5 mm (□), 10 mm (o), and 20 mm (◊). (b) $h_{l\text{-}l,0}$ = 10 mm, μ_{oil} = 0.131 Pa·s, Δp = 0.2 bar (□), 0.3 bar (o), and 0.4 bar (◊).*

Influence on the end state

In the tapping experiments, three different types of end states occurred, here named abnormal drainage, transitional drainage, and normal drainage. These types are defined by the conditions of the l-l interface level at the end of tapping. For the first type of tapping, abnormal drainage, the overall water level did not even descend to the outlet level but was above it at the termination of drainage (the top panel of Figure 22a). The horizontal blue line in subfigure (a) represents the level of the outlet. This pattern primarily occurred when the initial oil layer was thin. By contrast, in the normal drainage (bottom panel of subfigure a), the l-l interface descended clearly below the outlet in the end state and therefore bent upwards to the outlet. The transitional pattern is between these two extremes (middle panel of subfigure a), where the l-l interface was almost horizontal and its level was very close to the outlet level when the drainage ended. To investigate the effect of some process variables on the end interface state, six groups of drainage experiments were conducted for different initial oil-layer thicknesses (cf. Table 1). In every group, it was observed that abnormal drainage occurred for the case with a thin

initial oil layer, but with growing initial oil-layer thickness the tapping pattern evolved gradually through the transition to normal drainage patterns, which is demonstrated in Figure 22b. Thus, for each case, there is a particular initial oil-layer thickness, henceforth called the "critical oil layer thickness", for which the drainage ends with an l-l interface at the taphole level. If the initial oil-layer thickness exceeds the critical value, normal drainage will appear. Thus, a large critical oil-layer thickness means that abnormal drainage is more likely to occur.

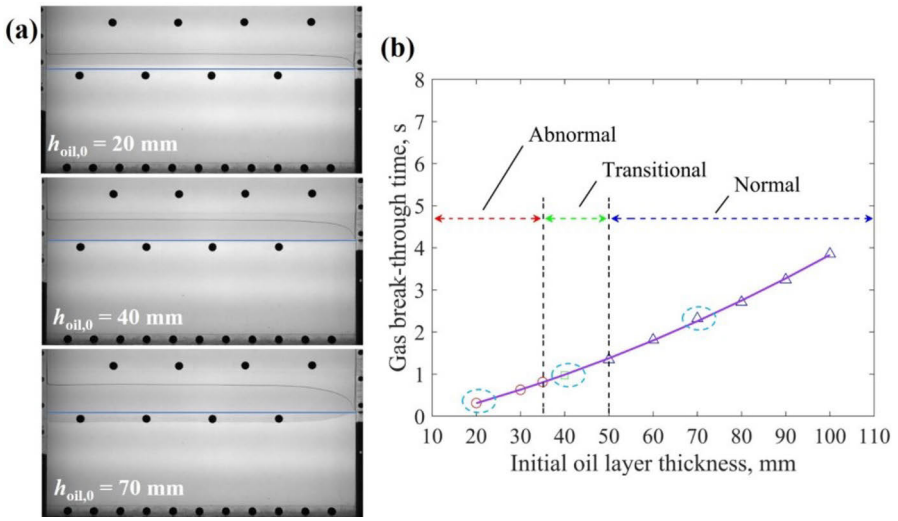

Figure 22. *(a) Drainage end state for abnormal drainage (top panel), transitional drainage (middle panel), and normal drainage (bottom panel) for three experiments with initial oil-layer thicknesses of 20 mm, 40 mm, and 70 mm, respectively. (b) Effect of initial oil layer thickness on the drainage end state.* $h_{l\text{-}l,0}$ *= 10 mm,* Δp *= 0.3 bar,* μ_{oil} *= 0.131 Pa·s.*

Two factors, the initial l-l interface level and pressure difference, are selected to show the influence on the drainage type in both dimensional and dimensionless form in Figure 23. Subfigure (a) demonstrates that the critical oil-layer thickness increased and the corresponding flow-out coefficient decreased with the initial l-l interface level. A possible explanation for this is that with the rise of the initial l-l interface, the initial outflow rate of water increases since water occupies the regions above and below the outlet, which makes the oil layer more prone to bend when oil starts to drain. The role of the pressure difference on the end state is depicted in Figure 23b, which shows that the critical oil-layer thickness increased with the pressure difference. As the pressure difference (working as a driving force for the tapping) increased, the flow rates of both liquids increased, increasing the descending speed of the l-l and l-g

interfaces. The bigger oil flow rate also increased the l-g interface bending, especially for the local interface near the outlet, leading to a shorter gas breakthrough time. Consequently, the critical oil-layer thickness increased. The lower panel of Figure 23b indicates that the flow-out coefficient corresponding to the critical oil-layer thickness was rather insensitive to the pressure difference.

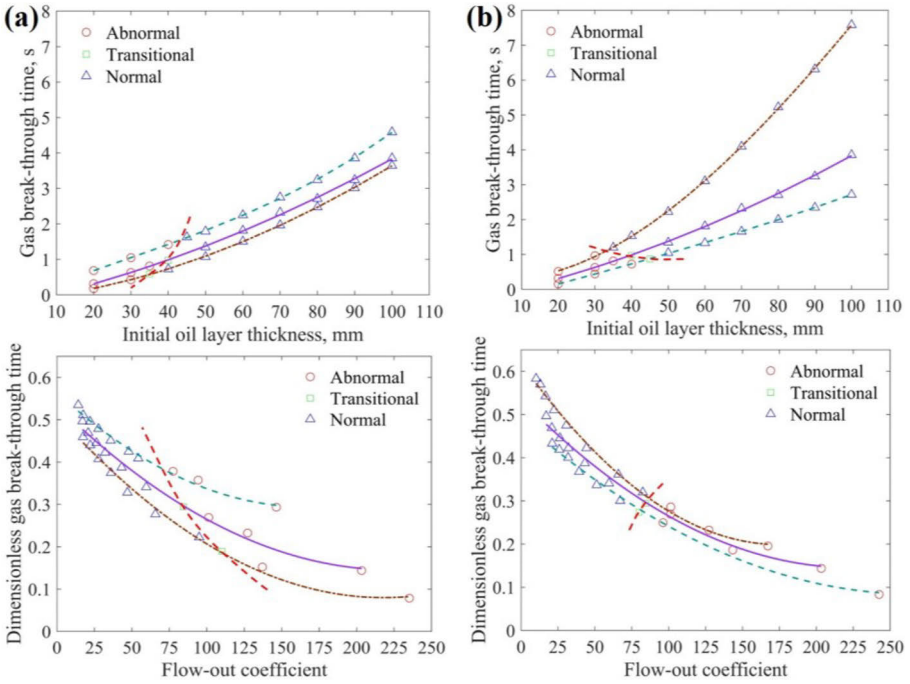

Figure 23. *(a) Effect of $h_{l\text{-}l,0}$ (5 mm: dash-dotted line, 10 mm: solid line, 20 mm: dashed line) on the drainage end state for Δp = 0.3 bar and μ_{oil} = 0.131 Pa·s. (b) Effect of Δp (0.2 bar: dash-dotted line, 0.3 bar: solid line and 0.4 bar: dashed line) on the drainage end state for $h_{l\text{-}l,0}$ = 10 mm and μ_{oil} = 0.131 Pa·s. Red dashed lines indicate states with transitional drainage.*

4.3. Quantitative analysis of hearth drainage experiments (Paper III)

To systematically undertake an accurate and quantitative analysis of the hearth drainage experiments, the digital image analysis technique proposed in Paper I was applied to interpret a series of tapping experiments undertaken at different operation conditions. The role of pressure difference, oil viscosity, initial l-l interface level, and initial oil-layer thickness on the evolution of liquid levels and volumes, oil ratios as well as interface angles were investigated in Paper III.

4.3.1. Experimental set-up and technique

A schematic of the experimental set-up is shown in Figure 16, which is the same experimental system used in Paper II. More details about the experimental set-up are described in Section 2.1 of Paper II and Paper III. After the experiments, all the recorded images were dealt with by the digital image analysis algorithm, based on the Matlab platform, to automatically extract desired information about the draining experiments. Compared to the algorithm proposed in Paper I, the approach used for bending-point detection was adjusted to improve the robustness. The bending points were here directly defined as the intersection points of the interfaces and a vertical reference line placed at a distance of one-tenth of the width (l) of the H-S model from the outlet (cf. Figure 24). Thus, during the drainage process, the horizontal positions of the bending points remain fixed. Information about other parts of the digital image analysis algorithm is given in Section 3 (especially in section 3.2.1-3.2.3) of Paper I and Section 2.2 of Paper III.

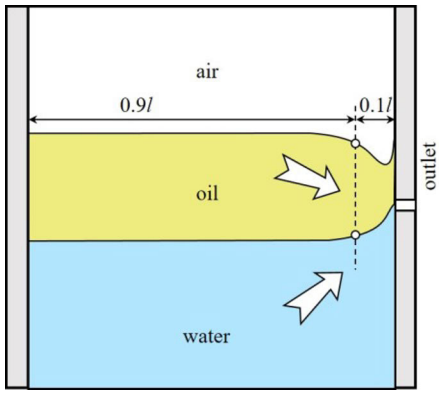

Figure 24. *Bending point locations applied in the study of Paper III.*

4.3.2. Experimental conditions

Like in the work of Papers I-II, water and engine oil were used in the H-S model. All the experimental conditions of the tapping experiments are listed in Table 3, in which the first experiment acts as a benchmark.

Table 3. *Experimental conditions with perturbed parameters written in bold.*

Experimental number	Δp (bar)	Oil viscosity (Pa·s)	Initial l-l interface level (mm)	Initial oil-layer thickness (mm)
1	0.3	0.131	10	100
2	**0.2**	0.131	10	100
3	**0.4**	0.131	10	100
4	0.3	**0.254**	10	100
5	0.3	0.131	**5**	100
6	0.3	0.131	**20**	100
7	0.3	0.131	10	**60**
8	0.3	0.131	10	**80**

4.3.3. Key findings and analysis

For a better comparison between experiments with different conditions, the liquid levels and volumes, liquid outflow rates, as well as oil ratio were depicted in both absolute and normalized time. The latter is defined as t/t_{total}, where t_{total} is the total tapping time. The influence of two process variables, initial oil-layer thickness, and pressure difference are shown below. The effect of the other two variables is not discussed here, but more information is presented in Paper III.

Effect on the evolution of liquid levels and volumes

The drainage under different conditions was investigated by depicting the time evolution of the liquid levels and volumes, calculated based on the interface locations extracted by the image processing algorithm.

Experiments 1, 7, and 8 (cf. Table 3) were conducted to investigate the effect of the initial oil-layer thickness. The evolution of the average liquid levels and liquid volumes is shown in Figure 25, in absolute (subfigure a) and normalized (subfigure b) time. The upper panel of subfigure (a) illustrates that the average l-g interface levels (upper red lines) evolve in parallel while the l-l interface levels evolve practically identically. The upper panel of subfigure (b) shows that the differences of the l-g interface levels at the end points are smaller and the average l-l interface level decreases with the initial oil-layer thickness, since the tapping time is longer for the cases with a thicker oil layer, so more oil and water can be drained. The lower panels of the figure demonstrate that the decrease of the oil volume is very small compared to the water and total volume,

which indicates that water is the main fluid in the total outflow. In addition, a thicker initial oil layer leads to more residual oil, but less water inside the model.

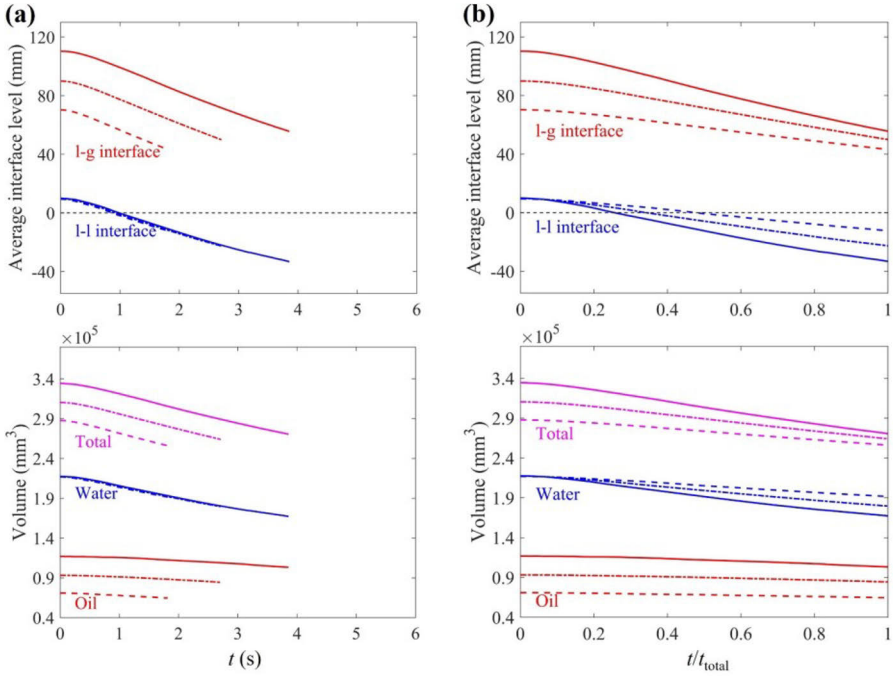

Figure 25. *Effect of initial oil-layer thickness in absolute (a) and normalized (b) time on average interface levels (upper panels) and liquid volumes (lower panels).* Δp *= 0.3 bar,* μ_{oil} *= 0.131 Pa·s,* $h_{l\text{-}l,0}$ *= 10 mm, initial oil-layer thickness* $h_{oil,0}$*: 60 mm (dashed line), 80 mm (dash-dotted line), 100 mm (solid line).*

Figure 26 describes how the pressure difference affects the evolution of the average interface levels and liquid volumes. The upper panels show that the descent rates of both interfaces increase with the pressure difference, but also that a faster tapping gives rise to more residual liquids when the tap ends, as also seen in the lower panels. Thus, a small pressure difference is beneficial for a more complete draining. However, in the real BF system, a low blast pressure would extend the tap duration, which limits the production rate of the furnace. Thus, a compromise solution must be considered in the practical operation.

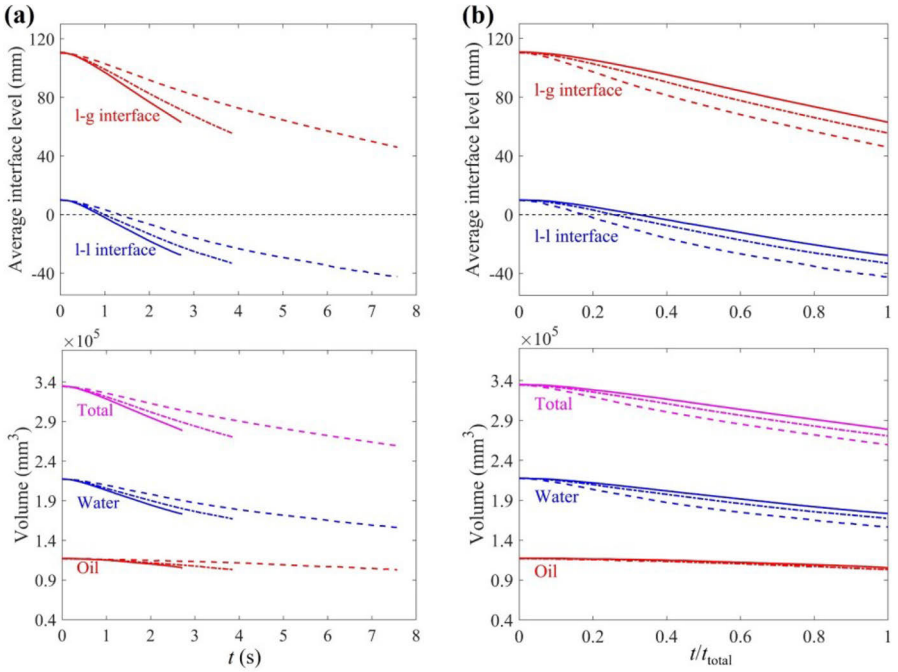

Figure 26. *Effect of pressure difference in absolute (a) and normalized (b) time on average interface levels (upper panels) and liquid volumes (lower panels).* $h_{oil,0}$ *= 100 mm,* μ_{oil} *= 0.131 Pa·s,* $h_{l\text{-}l,0}$ *= 10 mm,* Δp *= 0.2 bar (dashed line), 0.3 bar (dash-dotted line), 0.4 bar (solid line).*

Effect on the evolution of outflow rates and oil ratio

To gain a better understanding of the drainage, the evolution of the liquid outflow rates and the slag ratio in the outflow was studied. In the forthcoming analysis, the outflow rates and the oil ratio (i.e., the volume flowrate ratio of oil to water) are also described in absolute and normalized time.

Figure 27 depicts the effect of the initial oil-layer thickness on the evolution of the outflow rates and oil ratio. The upper panels show that increasing the initial oil-layer thickness gives rise to a smaller water outflow rate as the drainage approaches the end, while the oil outflow rate shows the opposite trend (but is not so clearly). Consequently, as seen in the lower panels, the oil ratio increases. The reason for this is that a thicker initial oil layer prolongs the tapping, which yields a lower l-l interface level near the end of the drainage and therefore a larger resistance to drain water.

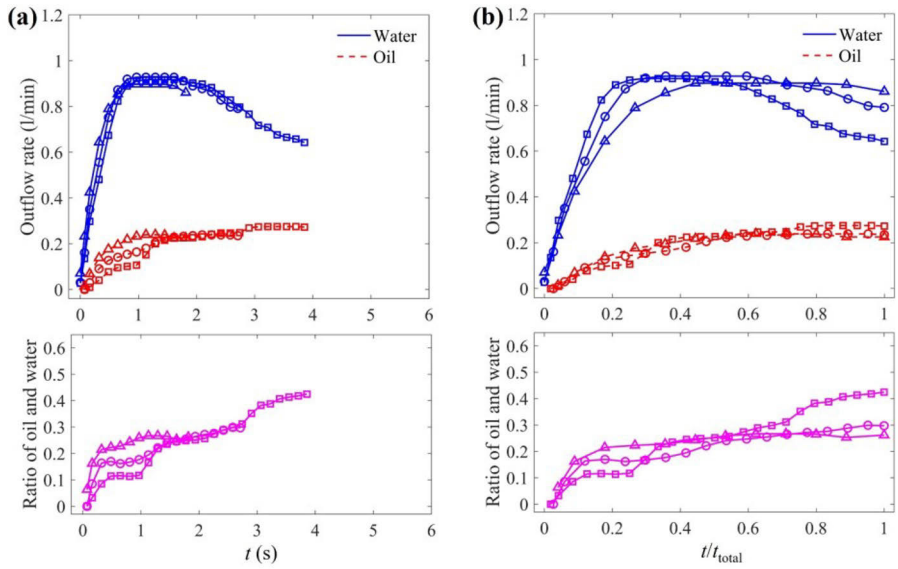

Figure 27. *Effect of initial oil-layer thickness in absolute (a) and normalized (b) time on the outflow rates (upper panels) and ratio of oil and water (lower panels).* $h_{l\text{-}l,0}$ *= 10 mm,* μ_{oil} *= 0.131 Pa·s,* Δp *= 0.3 bar,* $h_{oil,0}$ *= 60 mm (Δ), 80 mm (o) and 100 mm (□).*

The effect of the pressure difference on the outflow rates is depicted in the upper panels of Figure 28. Both oil and water outflow rates increase dramatically with the pressure difference. The lower panels demonstrate that the pressure difference has a very small influence on the evolution of the oil ratio in normalized time.

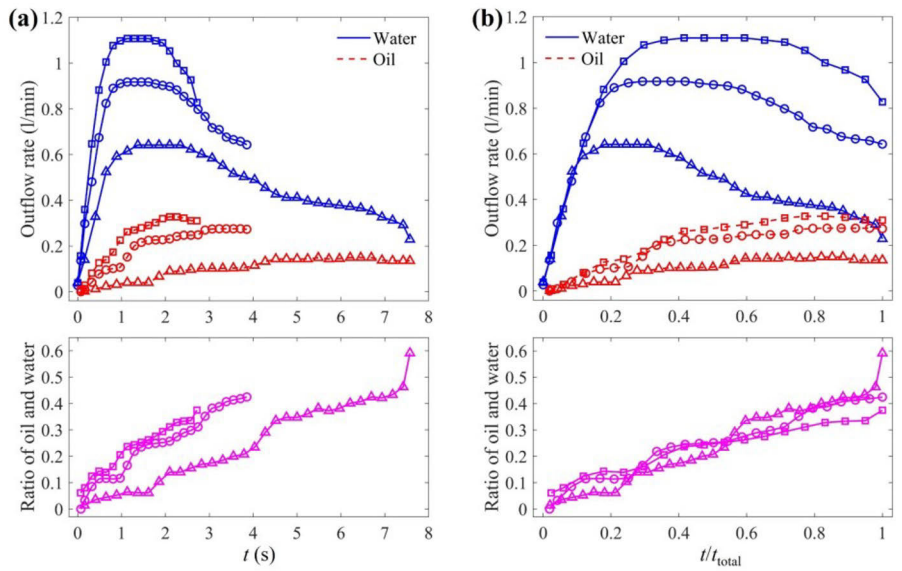

Figure 28. *Effect of pressure difference in absolute (a) and normalized (b) time on the outflow rates (upper panels) and ratio of oil and water (lower panels).* $h_{oil,0}$ *= 100 mm,* $h_{l\text{-}l,0}$ *= 10 mm,* μ_{oil} *= 0.131 Pa·s,* Δp *= 0.2 bar (Δ), 0.3 bar (o) and 0.4 bar (□).*

Effect on the evolution of interface angles

During the hearth drainage, the interface profiles and interface angle vary with the progress of tapping and are affected by some furnace process factors, such as blast pressure and dead man voidage. Detailed definitions of the l-g and l-l interface angles are presented in Section 4.3 of Paper III.

The role of the initial oil-layer thickness is first studied. The interface profiles are depicted in Figure 29b (upper row: 60 mm, middle row: 80 mm, lower row: 100 mm) for three different times distributed uniformly over the tapping (t/t_{total} = 1/3, 2/3, and 1). The evolution of interface angles is depicted in Figure 29a. Both sub-figures indicate that the l-l interface bending increases with the initial oil-layer thickness, since a thicker oil layer extends the draining and leads to a lower l-l interface. For the l-g interface, the changes in the bending angle are not significant. The time points selected in panel b are indicated by three dashed vertical lines in panel a. Note the different scales are used for the l-l (left) and l-g (right) interface angles in panel a.

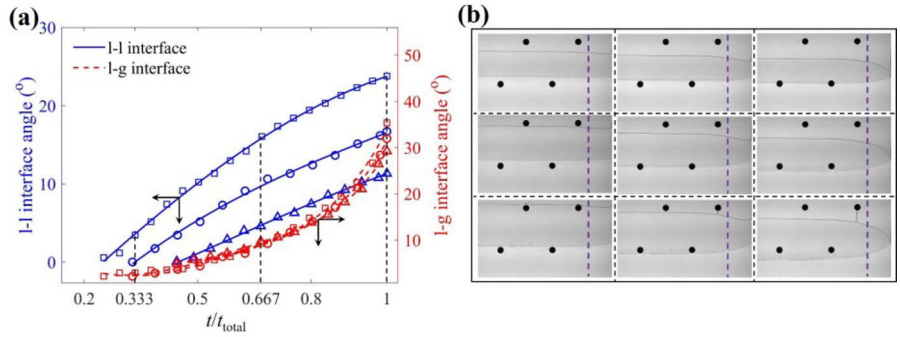

Figure 29. *Effect of initial oil-layer thickness on (a) the angles of l-g and l-l interfaces (Δ: 60 mm, o: 80 mm, □: 100 mm) and (b) on the interface bending (top: 60 mm, middle: 80 mm, bottom row: 100 mm). The subfigures of (b) show the states after one third (left), two thirds (center), and end (right) of the tapping process.* $h_{l\text{-}l,0}$ *= 10 mm,* Δp *= 0.3 bar and* μ_{oil} *= 0.131 Pa·s.*

Figure 30 shows that the l-g interface angle and the pressure difference have a notable positive correlation near the end of the draining, but the l-l interface angle shows an opposite trend. The former is attributed to a bigger pressure gradient in the oil phase, while the latter is because of a shorter tapping duration, leaving more water at the termination of the drainage. The end angle of the l-g interface is very close to 40° when Δp = 0.4 bar, which is the biggest interface angle encountered among all experiments reported in Paper III.

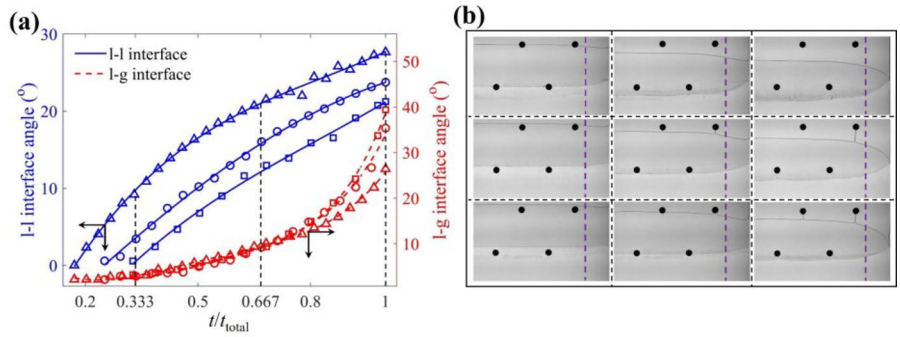

Figure 30. *Effect of pressure difference on (a) the angles of the interfaces (Δ: 0.2 bar, o: 0.3 bar, □: 0.4 bar) and (b) on the interface bending (top: 0.2 bar, middle: 0.3 bar, bottom row: 0.4 bar). The subfigures of (b) show the states after one third (left), two thirds (center), and end (right) of the tapping process.* $h_{oil,0}$ *= 100 mm,* $h_{l\text{-}l,0}$ *= 10 mm and* μ_{oil} *= 0.131 Pa·s.*

4.4. Numerical analysis of hearth drainage (Paper IV)

The H-S model is a nice experimental device to investigate hearth drainage due to the inherent advantages in flow visualization. However, a high labor cost is needed to conduct the experiments since the slot model has to be carefully cleaned between the experiments (for removing oil that sticks to the inside walls of the model). In addition, it is not easy to study certain factors, e.g., coke-free zone and dead man permeability. Considering these challenges and the advantages of computational models in terms of flexibility in adjusting the geometry and internal conditions, a VOF-based CFD model was developed to simulate the drainage in the H-S model that was used in Papers I-III by the author. For this model, the grid resolution was assigned carefully, and mesh dependency was also checked because both grid size and grid arrangement are important for an accurate interface shape description by the VOF method. The model was first validated by comparison with experimental data and then employed for studying the effect of several factors on the liquid levels and volumes, outflow rates, and interface bending.

4.4.1. Model description

Assumptions and simplifications

To simulate the water and oil flow behaviors in the H-S cell, the CFD modelling (Figure 31) was based on some fundamental assumptions and simplifications:

(a) All the fluids used in this model are incompressible and have constant density and viscosity.

(b) Heat transfer is not considered and the temperature is kept fixed (at 21 °C).

(c) The influences of capillary forces and surface tension are neglected.

(d) The fluids are pre-filled in the model before the simulation and the simulation will end when the air reaches the outlet channel.

(e) No liquids are added to the system during the drainage.

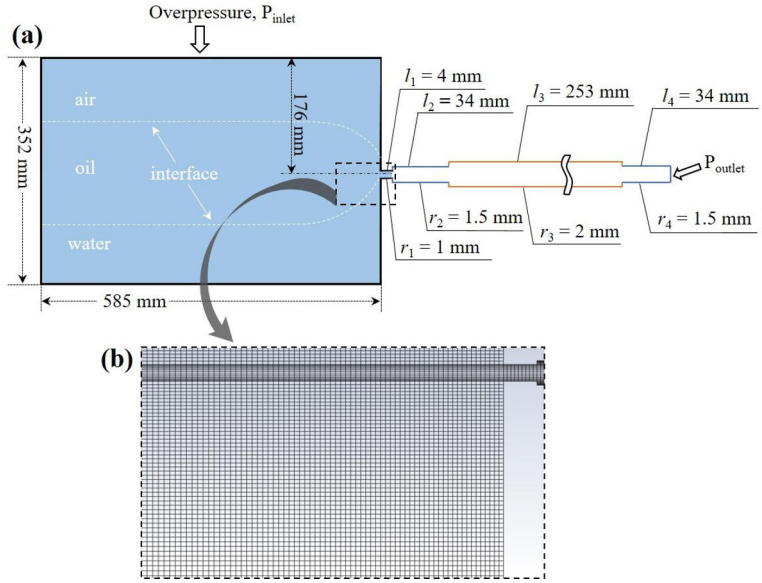

Figure 31. *Upper panel: The schematic of the CFD drainage model. Lower panel: The mesh resolution for the local region near the outlet.*

Model settings and model implementation

The computational domain and boundary conditions are illustrated schematically in Figure 31a. The main part of the model (the region with light blue color) is fully occupied by the particle-packed bed, except in the cases considering the effect of a coke-free zone. The outlet channel includes four parts and their lengths, *l*, and radius, *r*, are also illustrated in Figure 31a, which roughly correspond to the counterparts in the experimental work. Pressure boundary conditions are applied both for the inlet and outlet of the model, but with different values: a fixed overpressure is used in the inlet and the outlet is set as atmospheric pressure. The sidewalls and bottom are assumed to obey no-slip wall boundary conditions. The computational grid is distributed denser close to the outlet channel and in the outlet channel (cf. Figure 31b) to describe the local interface bending accurately.

ANSYS Fluent 2020 R1 was applied to solve all the used governing equations in the CFD model. The geometric reconstruction approach was employed to describe the l-l and l-g interfaces. Time steps and under-relaxation factors were set carefully to balance the overall calculation convergence and calculation time. The RNG k-ε turbulence model was applied to simulate the mean flow characteristics of the turbulent conditions since this model can describe the flow relatively accurately in both the low- and high-Reynolds regions.

4.4.2. Simulated cases and model validation

The drainage is affected by the operation conditions, such as blast pressure, dead man permeability, coke-free zone, and initially accumulated liquids. To understand this interaction of variables, eleven cases were simulated to examine the roles of the factors on the hearth drainage. The main conditions of the simulated cases are listed in Table 4, where the first case is the benchmark. The h_{cf} is the height of the coke-free zone that extends from the model bottom. Here, the top of the coke-free zone was simplified as a flat surface. The permeability of the packed bed (k) is determined by

$$k = b^2/12 \tag{12}$$

where $b = 2$ mm is the thickness of the H-S model used in the previous experimental work. Thus, the permeability for the base-case of the CFD model is $k = 0.333 \times 10^{-6}$ m^2.

Table 4. *Parameters for the simulation cases. Perturbed parameter values are written in bold.*

Case number	$h_{oil,0}$ (mm)	$h_{l\text{-}l,0}$ (mm)	Δp (bar)	$k \times 10^6$ (m^2)	h_{cf} (mm)
1	120	0	0.3	0.333	0
2	**100**	0	0.3	0.333	0
3	**140**	0	0.3	0.333	0
4	120	**– 20**	0.3	0.333	0
5	120	**+ 20**	0.3	0.333	0
6	120	0	**0.2**	0.333	0
7	120	0	**0.4**	0.333	0
8	120	0	0.3	**0.083**	0
9	120	0	0.3	**1.332**	0
10	120	0	0.3	0.333	**85**
11	120	0	0.3	0.333	**170**

A grid independence test was conducted and the tapping time was selected as the key index characterizing the hearth drainage to verify the CFD model. For the testing, the conditions ($h_{l\text{-}l,0}$ = 10 mm, $h_{oil,0}$ = 100 mm, Δp = 0.3 bar and μ_{oil} = 0.131 Pa·s) were set, which correspond to the base case of the earlier experimental study (cf. Table 2 of Paper III). Three grid resolution scales were examined: a coarse scale with 96000 cells, an

intermediate scale with 226901 cells, and a dense scale with 364987 cells. The corresponding tapping time was 3.55 s, 3.69 s and 3.65 s, respectively. As a compromise between computation cost and accuracy, the intermediate scale was chosen for the simulations.

To verify the model, a group of cases with different initial oil-layer thicknesses, $h_{oil,0}$, were simulated. The simulated results and associated experimental data are presented in Figure 32, which demonstrates a good agreement between the experimental and simulated tapping times (R^2 = 0.992).

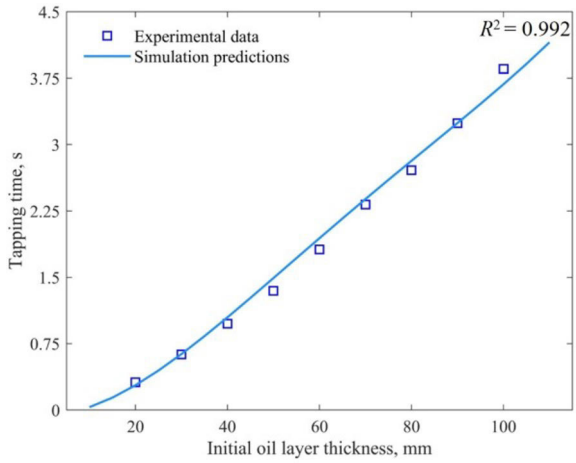

Figure 32. *Effect of initial oil-layer thickness on tapping time in the experiments (□) and simulations (—). Conditions: $h_{oil,0}$ = 10-110 mm, $h_{l\text{-}l,0}$ = +10 mm, Δp = 0.3 bar, $k = 0.333\times10^{-6}$ m² and h_{cf} = 0 mm.*

4.4.3. Key findings and analysis

The effect of initial oil-layer thickness, bed permeability, pressure difference, initial l-l interface level, and the extent of the coke-free zone on the drainage behaviors was examined in Paper IV. Here, the roles of the bed permeability and coke-free zone are reported.

Interface level and liquid volume evolution

Figure 33 shows the effect of different packed bed permeabilities (0.083×10^{-6} m², 0.333×10^{-6} m², and 1.332×10^{-6} m²) on the evolution of the liquid levels and volumes. Subfigure (a) demonstrates that a higher bed permeability increases the tapping duration and the oil outflow rate. A good bed permeability lowers the flow resistance and pressure drop in the packed bed, especially for the viscous oil, when the liquids flow through it. This leads to a more flat l-g interface during the drainage, which extends the tapping duration. In addition, a good bed permeability also enhances the oil outflow rate.

A higher bed permeability decreases the average l-g interface level and average l-l interface level at the end of drainage due to a longer draining time. This indicates that it is essential to keep the dead man permeable in the BF hearth to promote the drainage.

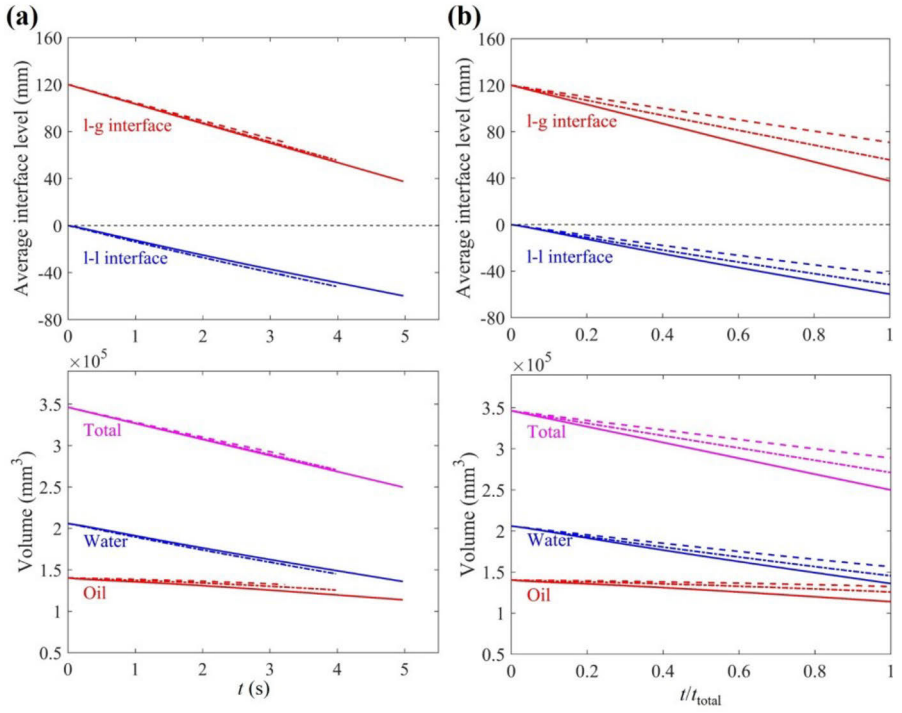

Figure 33. *Effect of bed permeability in absolute (a) and normalized (b) time on the interface levels (upper panels) and liquid volumes (lower panels).* $h_{oil,0}$ *= 120 mm,* $h_{l\text{-}l,0}$ *= 0 mm,* Δp *= 0.3 bar,* h_{cf} *= 0 mm, k = 0.083×10⁻⁶ m² (dashed line), 0.333×10⁻⁶ m² (dash-dotted line) and 1.332×10⁻⁶ m² (solid line).*

Figure 34 depicts the relation between the liquid levels (and volumes) and the height of the coke-free zone. Subfigure (a) shows that the coke-free zone has practically no influence on the drainage when it is not high enough to allow oil to pass through it during the drainage. These conclusions are identical to the findings by He et al. (2012). However, if the coke-free zone extends near the outlet level, it is possible to extract the oil through this zone, which prolongs the tapping significantly. The reason is that a lower pressure drop inside the oil phase decreases the bending of the l-g interface. The smaller oil flow resistance leads to a much bigger oil outflow rate. Thus, oil becomes dominant in the outflow, which finally leads to an end state with more residual water and less oil (cf. Figure 34b).

In the furnace hearth, the formation of the coke-free zone is the result of dead man floating. The dead man state depends on a balance of the forces acting on it. Because these forces change with the conditions, like the wear of the hearth bottom, the dead man may float or sit during different periods of the campaign.

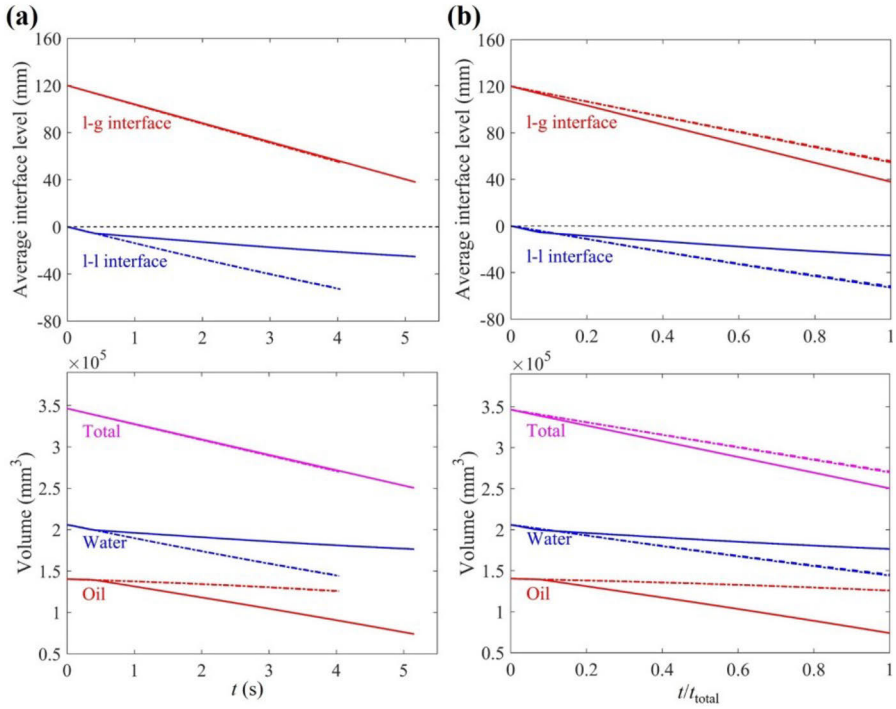

Figure 34. *Effect of the coke-free zone in absolute (a) and normalized (b) time on the average interface levels (upper panels) and liquid volumes (lower panels).* $h_{oil,0}$ *= 120 mm,* $h_{l\text{-}l,0}$ *= 0 mm,* Δp *= 0.3 bar,* $k = 0.333\times10^{-6}$ *m²,* h_{cf} *= 0 mm (dashed line), 85 mm (dash-dotted line) and 170 mm (solid line).*

Outflow rate and oil ratio evolution

The evolution of the outflow rates and oil ratio is depicted in Figure 35 for the cases with different bed permeabilities, i.e., 0.083×10^{-6} m², 0.333×10^{-6} m², and 1.332×10^{-6} m². A higher bed permeability increases primarily the oil outflow rate, since oil is the phase with higher viscosity, as shown in the upper panels. Naturally, this results in a larger oil ratio, as seen in the lower panels.

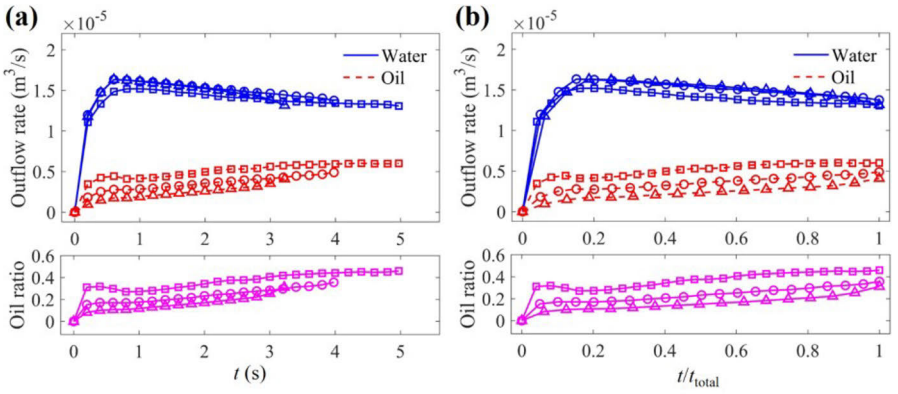

Figure 35. *Effect of bed permeability in absolute (a) and normalized (b) time on the outflow rates (upper panels) and ratio of oil and water (lower panels).* $h_{oil,0}$ *= 120 mm,* $h_{l\text{-}l,0}$ *= 0 mm,* Δp *= 0.3 bar,* h_{cf} *= 0 mm, k = 0.083×10⁻⁶ m² (Δ), 0.333×10⁻⁶ m² (o) and 1.332×10⁻⁶ m² (□).*

Figure 36 demonstrates how the coke-free zone affects the outflow rates and oil ratio. It is seen that coke-free zone does not have an effect until extending (close) to the outlet, but if it does, the oil outflow rate and oil ratio increase significantly and oil is the main phase that is drained.

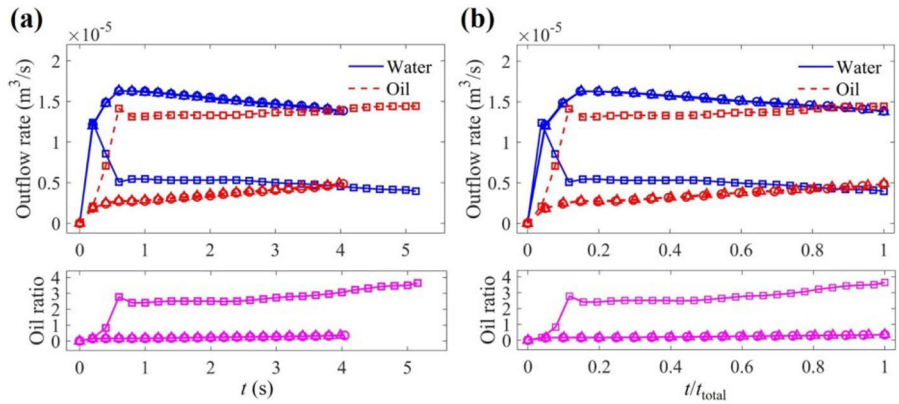

Figure 36. *Effect of the coke-free zone in absolute (a) and normalized (b) time on the outflow rates (upper panels) and ratio of oil and water (lower panels).* $h_{oil,0}$ *= 120 mm,* $h_{l\text{-}l,0}$ *= 0 mm,* Δp *= 0.3 bar, k = 0.333×10⁻⁶ m², h_cf = 0 mm (Δ), 85 mm (o) and 170 mm (□).*

Interface angle evolution

Figure 37b depicts the influence of the bed permeability on the interface bending at three different times distributed uniformly over the tapping (t/t_{total} = 1/3, 2/3, and 1). The corresponding evolution of the interface

angles is depicted in Figure 37a. They demonstrate that higher bed permeability decreases the bending degree of both interfaces clearly, especially for the l-g interface. Viscous fingering of the l-g interface appeared for the case with a low bed permeability (cf. rightmost panel in the top row of Figure 37b). This led to a clearly shorter tapping time, which emphasizes the importance of maintaining a high hearth permeability.

The relation between interface bending and the height of the coke-free zone is shown in Figure 38. It illustrates that the effect is not clear except when the coke-free zone is high enough to allow oil to flow through it. When oil is drained out through the coke-free zone, both interfaces bend clearly less. This indicates the important role of the pressure drop in the more viscous phase (oil) close to the outlet on the interface bending, as also concluded by Roche et al. (2019).

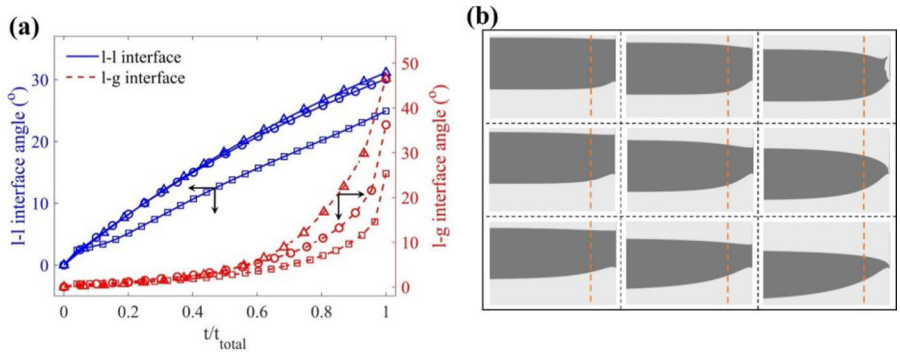

Figure 37. *Effect of packed bed permeability on (a) the angles of l-g and l-l interfaces during the tapping (Δ: 0.083×10⁻⁶ m², o: 0.333×10⁻⁶ m², □: 1.332×10⁻⁶ m²) and (b) on interface bending (upper row: 0.083×10⁻⁶ m², middle row: 0.333×10⁻⁶ m², lower row: 1.332×10⁻⁶ m²). The subfigures of (b) show the states after one third (left), two thirds (center), and end (right) of the tapping process.* $h_{oil,0}$ *=120 mm,* $h_{l\text{-}l,0}$ *= 0 mm,* Δp *= 0.3 bar and* h_{cf} *= 0 mm.*

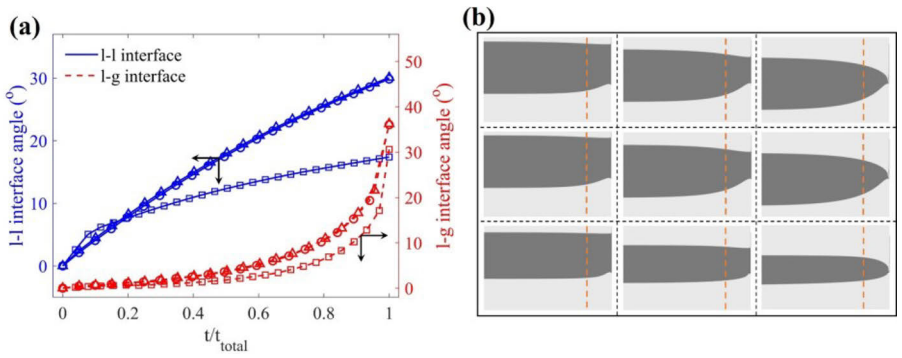

Figure 38. *Effect of coke-free zone on (a) the angles of l-g and l-l interfaces (Δ: 0 mm, o: 85 mm, □: 170 mm) and (b) on the interface bending (upper row: 0 mm, middle row: 85 mm, lower row: 170 mm). The subfigures of (b) show the states after one third (left), two thirds (center) and end (right) of the tapping process.* $h_{oil,0}$ *= 120 mm,* $h_{l\text{-}l,0}$ *= 0 mm,* Δp *= 0.3 bar and* $k = 0.333 \times 10^{-6}$ *m²*.

4.5. Asymptotic model of the hearth erosion (Paper V)

To provide a theoretical estimation of the asymptotic inner profile of the hearth, a CFD-based model was developed to estimate the iron flow, refractory erosion, and possible skull in steady state. The profile, shaped by the flowing hot metal, skull, and remaining lining is obtained based on the calculated fluid flow and temperature distribution in the domain. The model can be used as a tool to assess the potential strengths and weaknesses of a specific hearth design, and also to analyze the effect of the boundary conditions on the final lining state.

4.5.1. Model outline

Compared with the commonly used CFD-based BF hearth models, where the solid-liquid interface is fixed, the current model considers the moving of interfaces between the different phases during the calculation cycle to achieve an asymptotic state. For the analysis, the commonly accepted concept of the 1150 °C isotherm as the boundary between the hot metal and the solid zone was applied (Geerdes et al. 2015): this is the lowest temperature at which carbon-saturated iron can be found in the liquid state and thus an absolute limit for the maximum iron penetration into the lining (Torrkulla and Saxén, 2000). Figure 39 shows the basic principles of the model and how the hearth-internal profile is updated. Details about the model are given in Section II of Paper V.

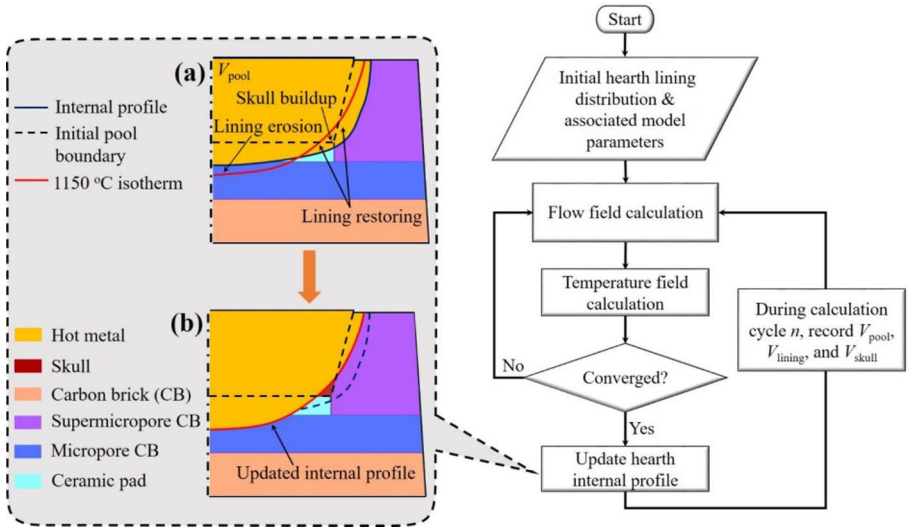

Figure 39. *Principles of updating procedure for the internal hearth profile based on the 1150 ℃ isotherm. (a) Initial guess of the internal hearth profile and (b) updated profile.*

The macroscopic governing equations for fluid flow in an (isotropic) packed bed are used to represent the flow in the hearth. The equations for continuity and momentum balance are written as

$$\nabla \cdot (\varepsilon \rho \mathbf{u}) = 0 \tag{13}$$

$$\nabla \cdot (\varepsilon \rho \mathbf{u}\mathbf{u}) = \nabla \cdot (\varepsilon \eta \nabla \mathbf{u}) + \varepsilon(\rho \mathbf{g} - \nabla p - \mathbf{R}) \tag{14}$$

where ε, ρ, η, $\mathbf{u}$, $\mathbf{g}$, and p are the dead man porosity, liquid density, viscosity, velocity vector, gravity vector, and pressure. The last term on the right-hand side of Eq. (14) describes the flow resistance of the dead man and is expressed by the well-known Ergun equation

$$\mathbf{R} = \frac{\varepsilon}{A}\eta \mathbf{u} + \frac{\varepsilon^2 B}{2}\rho \mathbf{u}|\mathbf{u}| \tag{15}$$

where A is the permeability of the dead man and B is the inertial term accounting for the kinetic energy of turbulent eddies, which can be generated within the void space when the flow rate is relatively high. The two parameters are given by

$$A = \frac{d_{\text{coke}}^2}{150}\frac{\varepsilon^3}{(1-\varepsilon)^2};\ B = \frac{3.5}{d_{\text{coke}}}\frac{1-\varepsilon}{\varepsilon^3} \tag{16a, b}$$

where d_{coke} is the coke particle diameter. For the present work, the coke particle size is supposed to be fixed and one common particle diameter in

the hearth, 35 mm, is used in the model. However, in the real BF hearth, the sizes of the coke particles are not uniform (cf. Post, 2019).

The energy conservation equation for the liquid phase can be written as

$$\nabla \cdot (\mathbf{u}T) - \nabla \cdot \left(\frac{\lambda}{\rho c_{\mathrm{P}}} \nabla T\right) = 0 \tag{17}$$

where T, λ, and c_{p} are the temperature, thermal conductivity and heat capacity, respectively, and the term $\alpha = \lambda/(\rho c_{\mathrm{p}})$ is the thermal diffusivity. Inspection of this equation reveals that it is identical with the Laplace equation of heat conduction if the first (i.e., convective) term on the left-hand side is zero, so the equation is also applicable to the solid phase (wall and skull) with a special treatment on the flow field. This reduces the model complexity provides a means of tracking the liquid-solid front in an iterative solution of the problem by employing a unified form of the energy equation to both phases. Flow suppression can be accomplished by zeroing the velocity in the computational cells located in the solid zone. As this would cause severe convergence problems due to a violation of the continuity equation, the computational flow field in the solid zone was instead strongly suppressed by giving the porosity in a very small value in Eq. (15), which yields an appreciable momentum sink in Eq. (14). Analysis of the model suggested that a porosity of $\varepsilon = 10^{-4}$ resulted in velocity of 10^{-15} m/s or less in the solid zone.

The model is two-dimensional for fast computation. The hearth geometry and lining structure studied are depicted in Figure 40, which are based on the hearth of a reference furnace, using the following boundary conditions. For the momentum equations, a constant and uniform inlet velocity of hot metal is given at ①. Non-slip wall conditions are given at ②–④, and constant pressure is applied at the outlet ⑤. For the energy equation, a constant temperature of hot metal is set along boundary ① and the top surface of ② is assumed to be adiabatic. Constant temperatures are applied at boundaries ③ and ④, but the model is compatible with other thermal conditions as well (e.g., heat flux, thermal radiation, or forced convection) and different velocity profiles at ①.

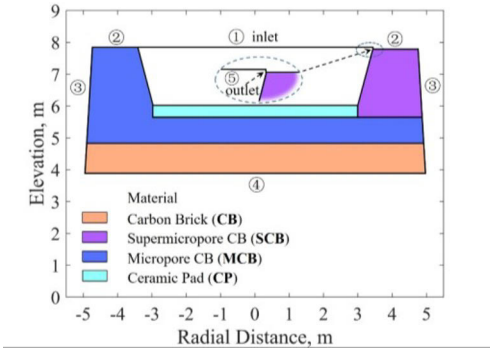

Figure 40. *Dimensions and lining design of the hearth as well as boundary (referred to by ①–⑤) conditions used in the model.*

4.5.2. Model application

To illustrate results of the model, the base case was selected as an example and its hearth profile, hot metal streamlines and temperature distribution are shown in Figure 41. The general flow pattern of the hot metal and the hearth erosion profile are presented in Figure 41a. The lining profile exhibits a "bowl-shaped" erosion type that has also been encountered in practice. Very little skull is formed and only at the joint between the left sidewall and ceramic pad: the skull formation is facilitated by a low velocity of the iron. This also agrees well with operation experience and with the guidelines for BF hearth design. Figure 41b depicts the thermal contours, which show that the temperature distributes uniformly in the liquid pool, while a high temperature gradient appears in the solid materials since they have considerably lower heat conductivities.

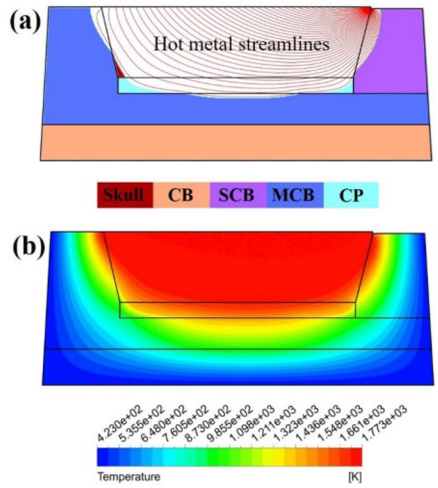

Figure 41. *Hearth profile (a) and temperature distribution (b) for the base case.*

4.5.3. Key findings and analysis

A series of cases (cf. Table 5) with a wide range of operating conditions were simulated to estimate their influence on the asymptotic hearth erosion state. The first row of the table (Case 1.1) is the base case. Here, the outer surfaces of the bottom and sidewall of the hearth were set to 423 K (150 °C), since the computational domain has omitted the outermost lining layers (ramming mass, furnace shell, etc.).

A summary of the quantitative analysis for Cases 1.1-1.9 is listed in Table 6, where the erosion ratio of the different lining materials is reported: the erosion ratio is defined as the ratio between the amount of eroded material and the intact material at the starting states. Also, erosion depth in three locations is reported, with the points depicted in Figure 42. The results demonstrate the efficiency of a ceramic pad (CP) to withstand erosion since it serves as a "thermal barrier" separating the high-temperature liquid and the bottom lining. The findings also indicate how hearth erosion can be restrained by lowering the production rate or reducing hot metal temperature. Naturally, the former strategy affects the production economics of the plant strongly, while for the latter the downstream processing and slag fluidity may be disturbed. The success of the approach to control wear by affecting the coke-bed porosity seems limited even though center charging of high-quality and relatively inert coke has been suggested as one useful method (Yu and Shen, 2019). The influence of the cooling conditions was found relatively small, which agrees with the findings by Kumar (2005). One possible reason is that the ceramic pad restrains the effect of the hearth bottom temperatures due to its very low thermal conductivity.

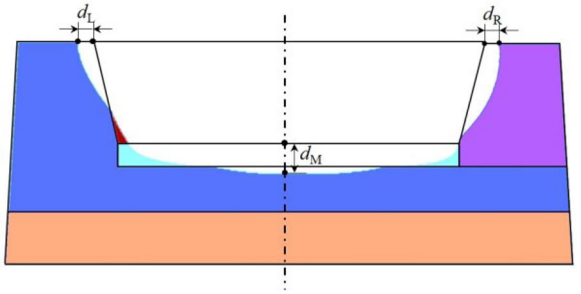

Figure 42. *Schematic of the three erosion depths at different locations.*

Table 5. *The effect of the operating conditions on hearth erosion and skull buildup. Sidewall refers to ③ and bottom to ④ in Figure 40.*

Case No.	Inlet velocity $\times 10^4$ (m/s)	Dead man porosity (-)	Inlet temp. of hot metal (K)	Sidewall temp. (K)	Bottom temp. (K)
1.1	1.0	0.3	1773	423	423
1.2	**0.5**	0.3	1773	423	423
1.3	**1.5**	0.3	1773	423	423
1.4	1.0	**0.1**	1773	423	423
1.5	1.0	**0.5**	1773	423	423
1.6	1.0	0.3	**1723**	423	423
1.7	1.0	0.3	**1823**	423	423
1.8	1.0	0.3	1773	**523**	423
1.9	1.0	0.3	1773	423	**523**

Table 6. *Erosion ratios (%) of different refractory materials and erosion depths for Cases 1.1-1.9.*

Case No.	CP	MCB	SCB	d_L (m)	d_M (m)	d_R (m)
1.1	85.1	4.3	12.4	0.268	0.501	0.249
1.2	53.3	0.5	4.8	0.128	0.297	0.152
1.3	95.6	15.8	20.4	0.376	0.749	0.313
1.4	71.5	1.1	10.0	0.182	0.351	0.216
1.5	91.3	10.3	15.0	0.333	0.652	0.270
1.6	71.7	1.1	9.4	0.182	0.351	0.216
1.7	92.2	11.0	16.0	0.333	0.652	0.270
1.8	88.0	6.3	14.9	0.333	0.533	0.281
1.9	89.8	8.7	13.1	0.268	0.641	0.249

To examine how the thermal conductivities of the different lining materials affect the asymptotic hearth erosion state, one more group of cases were also simulated and analyzed (in part B of Section III of Paper V). As an example, the effect of microporous carbon brick is treated here. The microporous carbon brick (blue region) is used both in the sidewall

opposite the taphole and in the bottom below the ceramic pad, so the effect of its thermal conductivity is more complicated than the other cases. The original value was halved (Case b in Figure 43) or doubled (Case c in Figure 43), yielding the results in Figures 43b and 43c. The former case (λ_{MCB} = 5.3 W/(m·K)) leads to a very "bowl-shaped" hearth profile, where the sidewall on the taphole side is only slightly worn, while the latter case results in practically no wear of, but instead a quite considerable skull formation on the lower sidewall opposite the taphole, and a flatter bottom profile.

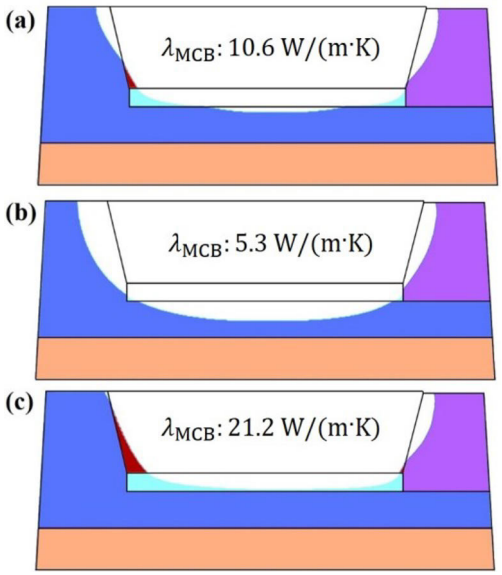

Figure 43. *Effect of thermal conductivity of the micropore carbon brick (blue region) on the asymptotic hearth state. Conditions:* λ_{CP}: 2.0 $W/(m{\cdot}K)$, λ_{SCB}: 20.5 $W/(m{\cdot}K)$, λ_{CB}: 7.2 $W/(m{\cdot}K)$, λ_{MCB}: 10.6 $W/(m{\cdot}K)$ *(a),* 5.3 $W/(m{\cdot}K)$ *(b),* 21.2 $W/(m{\cdot}K)$ *(c).*

The model can also be used to study the influence of adjusting the furnace operation conditions on the erosion state, starting from an asymptotic state predicted by the model. The details of this study are given in part C of Section III of Paper V but one example is presented here. The model was first to run to the asymptotic state using the base-case setup, after which a decrease in the iron inlet velocity to 0.05 mm/s was implemented, and the model was run to a new steady state. The simulation results are illustrated in Figure 44, where the end state of the base case (Figure 44a) represents the starting state of the revised operation periods, leading to the results depicted in Figure 44b. The parameters of the erosion depths

for the two states are: Case a in Figure 44: d_L = 0.268 m, d_M = 0.501 m, d_R = 0.249 m; Case b in Figure 44: d_L = 0.204 m, d_M = 0.329 m, d_R = 0.184 m. The reduction in the production rate is seen to result in a skull layer that covers the whole hearth, thus protecting the lining.

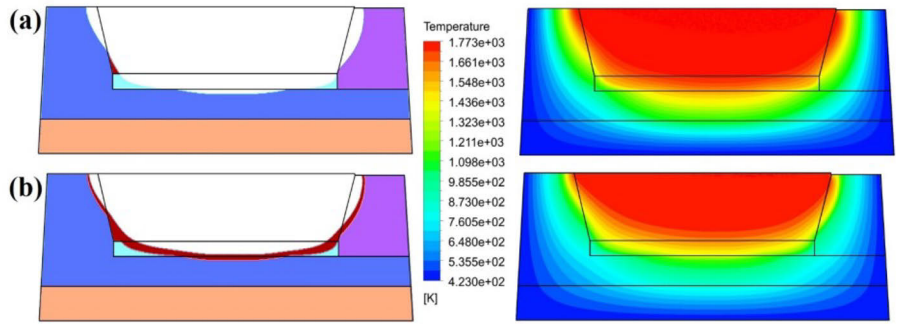

Figure 44. *(a) Erosion profile and temperature contours of base case, which acts as the starting point for the new calculations. (b) New erosion profile and temperature contours after halving the iron inlet velocity.*

It also should be pointed out that the model only considers hearth erosion from a thermal perspective and considers neither mechanical wear nor stress. Further, as the model is static, it simplifies the view. On the other hand, this makes it possible to use it on a routine basis for sensitivity analysis without prohibitive computational demand. The main potential of the model lies in its use as a tool for assessing the role of different factors in the design of the hearth refractory and operation. However, since the model has been simplified in many aspects compared with the practical BF, it is not easy to make quantitative comparisons of its results with practical findings.

5. Conclusions

The main purpose of this thesis work was to investigate the iron and slag flow in the BF hearth for gaining a deeper understanding of the complex hearth-drainage phenomena and the process of lining wear. Both experimental and simulation models were employed for a systematic and quantitative analysis.

An H-S model, i.e., a quasi-two-dimensional system with fluids enclosed by two rectangular and transparent walls, was constructed for studying BF hearth drainage. The approach is based on the analogy between the flow between two such plates and that in a system with a packed bed of particles. This design makes it is easy to observe and record the fluid interfaces during the draining with low optical distortion. Section 4.1 (Paper I) outlines a digital image analysis algorithm to automatically deal with information from the tapping experiments in the H-S model. The image analysis method consists of three modules, i.e., image pre-processing, interface extracting, and bending point detection, where the interface extraction is the core part. The developed algorithm was validated and then employed for extracting information from tapping experiments. Finally, based on the algorithm, the evolution of the liquid levels and volumes, liquid outflow rates and oil ratio, as well as interface bend ratios and angles was analyzed for a drainage experiment to illustrate the application of the algorithm in the quantitative analysis.

In Section 4.2 and Paper II, a series of experiments were conducted in the H-S model to study the roles of the initial amount of liquids, blast pressure, and slag viscosity on the drainage behaviors and the corresponding interface behaviors. After the experiments, the experimental results were processed by the digital image analysis method to extract key draining information, i.e., tapping time, residual liquid ratios, and l-l interface end state. To compare the present experimental results with the findings from the practical BF system, the results were studied in dimensionless form. The key findings of this part of the work were that the tapping duration extended and the residual ratios of both liquids decreased with the initial liquid-liquid and liquid-gas levels, and with the slag viscosity, while tapping duration decreased with the blast pressure.

In Section 4.3 (Paper III) and Section 4.4 (Paper IV), a more quantitative analysis of hearth drainage was undertaken by experiments and simulation. The experiments were conducted in the H-S model to study the role of initial molten liquid amounts, slag viscosity, and blast pressure on the hearth tapping. Section 4.4, a CFD model was developed for simulating the H-S model. The computational model was verified by the data from the experimental counterpart. The CFD approach saves labor

cost of the experiments and also makes it is feasible to examine the effect of certain process variables, such as bed permeability and the height of a coke-free zone. By employing both models, at different operational conditions, the evolution of the process variables, i.e., liquid levels and volumes, liquid outflow rates and oil ratio, as well as interface angles was finally analyzed to characterize the drainage behavior. The study has highlighted some important factors in the practical operation of the BF hearth. 1) A good coke-bed permeability is necessary for efficient slag drainage; by well-mastered outflow rates, an excessive bending of the slag-gas interface during the later parts of the tappings can be avoided. 2) The residual slag ratio is not crucially dependent on the iron-slag level in the blast furnace hearth at tap start. 3) The effect of the coke-free zone on the hearth drainage is not distinct unless it extends close to the taphole.

In Section 4.5 and Paper V, an asymptotic hearth erosion model based on CFD was established, which considers fluid flow, heat transfer, refractory erosion, and possible skull buildup simultaneously during the calculation. For this model, both lining and skull profiles are moved during the calculation cycle until a stable state is reached, which is taken to correspond to the asymptotic state of the hearth. The algorithm developed realizes a straightforward and efficient tracking of the liquid-solid interface. The assumptions behind the model, its main equations, and the solution procedure have been described. To show the applicability and versatility of the model, a series of illustrative cases was analyzed. The model can be applied as a tool to assess the potential merits and drawbacks of a specific hearth design with respect to hearth durability. It is also possible to use the model to examine how the hearth lining erosion state would be affected if the operating conditions are adjusted.

6. Future prospects

The work in the thesis has shed light on some aspects of BF hearth drainage and erosion, and has deepened the understanding of the factors that influence the performance of the hearth. Still, more studies are required to clarify issues that remain open. For the drainage experiments, it would be necessary to conduct trials in a three-dimensional model, since there are some limitations of the two-dimensional approach. For instance, the bending of the interfaces close to the taphole is fundamentally different in two and three dimensions due to the effect of the geometry on the fluid volumes. However, how to extract the detailed draining information accurately from the draining experiments in a three-dimensional model is still an open issue.

As for the CFD tapping model, some possible extensions are to simulate quasi-stationary operation with production of liquids and intermittent drainage from one outlet, or alternating draining from two (opposite) outlets. Possible developments of the asymptotic erosion model are to consider a coke-free zone under the dead man, which would simultaneously make it possible to determine the floating state of the dead man by a force balance.

References

Agrawal, A., Kor, S. C., Nandy, U., Choudhary, A. R. and Tripathi, V. R. (2016), "Real-time blast furnace hearth liquid level monitoring system", *Ironmaking and Steelmaking,* vol. 43, pp. 550–558.

Alter, M. A., Brunner, J. M. and Holmes, D. J. (2013), "Continuous monitoring of liquid level and thermal state in the hearth based on measurement of emf on the blast furnace shell", *Iron and Steel Technology*, vol. 10, pp. 43–50.

Andreev, K., Louwerse, G., Peeters, T. and van der Stel, J. (2017), "Blast furnace campaign extension by fundamental understanding of hearth processes", *Ironmaking and Steelmaking*, vol. 44, pp. 81–91.

Ashrafian, A and Johansen, S. T. (2006), "Tapping of stratified liquids from a packed bed", Fifth International Conference on CFD in the Process Industries, CSIRO, Melbourne, Australia.

Bambauer, F., Wirtz, S., Scherer, V. and Bartusch, H. (2018), "Transient DEM-CFD simulation of solid and fluid flow in a three dimensional blast furnace model", *Powder Technology*, vol. 334, pp. 53–64.

Bear, J. (1972), *Dynamics of Fluids in Porous Media*, 1st ed., American Elsevier Company, New York, USA.

Bean, I. (2008), *Blast Furnace Hearth Drainage Improvement of the Residual-Flowout Correction*, Master's Thesis, University of New South Wales, Sydney, Australia.

Biswas, A. K. (1981), *Principles of blast furnace ironmaking: theory and practice*, Cootha, Brisbane, Australia.

Brännbacka, J. and Saxén, H. (2001), "Modeling the Liquid Levels in the Blast Furnace Hearth", *ISIJ International*, vol. 10, pp. 1131-1138.

Brännbacka, J. and Saxén, H. (2003), "Model Analysis of the Operation of the Blast Furnace Hearth with a Sitting and Floating Dead Man", *ISIJ International*, vol. 43, pp. 1519-1527.

Brännbacka, J. and Saxén, H. (2004), "Novel model for estimation of liquid levels in the blast furnace hearth", *Chemical Engineering Science*, vol. 59, pp. 3423-3432.

Brännbacka, J. (2004), *Model Analysis of Dead-man Floating State and Liquid Levels in the Blast Furnace Hearth*, Doctoral thesis, Åbo Akademi University, Turku, Finland.

Brännbacka, J. and Saxén, H. (2008), "Model for Fast Computation of Blast Furnace Hearth Erosion and Buildup Profiles", *Industrial & Engineering Chemistry Research,* vol. 47, pp. 7793-7801.

Bolf, N. (2004), "Application of infrared thermography in chemical engineering", *Journal of Chemists and Chemical Engineers*, vol. 53, pp. 549-555.

Cameron, I., Sukhram, M., Lefebvre, K. and Davenport, W. (2020), *Blast Furnace Ironmaking: Analysis, Control, and Optimization*, 1st ed., Elsevier.

Chibwe, D. K., Evans, G. M., Doroodchi, E., Monaghan, B. J., Pinson, D. J. and Chew, S. J. (2020), "Charge material distribution behaviour in blast furnace charging system", *Powder Technology*, vol. 366, pp. 22-35.

Dash, S. K., Ajmani, S. K., Kumar, A. and Sandhu, H. S. (2001), "Optimum Taphole Length and Flow Induced Stresses", *Ironmaking and Steelmaking*, vol. 28, pp. 110-116.

Dash, S. K., Jha, D. N., Ajmani, S. K. and Upadhyaya, A. (2004), "Optimisation of Taphole Angle to Minimise Flow Induced Wall Shear Stress on the Hearth", *Ironmaking*

and Steelmaking, vol. 31, pp. 207-215.

Dong, X. F. and Zulli, P. (2020), "Prediction of blast furnace hearth condition: part I - a steady state simulation of hearth condition during normal operation", *Ironmaking and Steelmaking*, vol. 47, pp. 307-315.

Fukutake, T. & Okabe, K. (1976), "Experimental Studies of Slag Flow in the Blast Furnace Hearth during Tapping Operation", *Transactions of the ISIJ*, vol. 16, pp. 309-316.

Fu, D., Chen, Y. and Zhou, C. Q. (2015), "Mathematical modeling of blast furnace burden distribution with non-uniform descending speed", *Applied Mathematical Modelling*, vol. 39, pp. 7554-7567.

Gao, K., Jiao, K. X., Zhang, J. L., Zhang, L., Wang, C., Gong, W. M., Zheng, J. X. and Zhang, H. B. (2020), "Dissection investigation of forming process of titanium compounds layer in the blast furnace hearth", *ISIJ International*, vol. 60, pp. 2385-2391.

Geerdes, M., Chaigneau, R. and Kurunov, I. (2015), *Modern Blast Furnace Ironmaking: An Introduction*, 3rd ed., IOS Press.

Gonzalez, M. and Goldschmit, M. B. (2006), "Inverse geometry heat transfer problem based on a radial basis functions geometry representation", *International Journal for Numerical Methods in Engineering,* vol. 65, pp. 1243-1268.

Gomes, F. S. V., Salles, J. L. F. and Wasem, L. A. (2011), "A new prediction model for liquid level in blast furnaces based on time series analysis", *Proceedings of the IEEE International Conference on Control and Automation*, Santiago, Chile, pp. 772–777.

Gomes, F. S. V., Côco, K. F. and Salles, J. L. F. (2017), "Multistep Forecasting Models of the Liquid Level in a Blast Furnace Hearth", *IEEE Transactions on Automation Science and Engineering*, vol. 14, pp. 1286-1296.

Guo, B. Y., Maldonado, D., Zulli, P. and Yu, A. B. (2008), "CFD Modelling of Liquid Metal Flow and Heat Transfer in Blast Furnace Hearth", *ISIJ International*, vol. 48, pp. 1676-1685.

Hattink, M., van der Stel, J. and Lecacheux, B. (2011), *Determination of Factors Influencing the Deadman Position and Evaluation of Its Impact on Blast Furnace Lifetime*, Final report, European Commision, KI-NA-24976-EN-N.

He, Q., Zulli, P., Tanzil, F., Lee, B., Dunning, J. and Evans, G. (2002), "Flow Characteristics of a Blast Furnace Taphole Stream and Its Effects on Trough Refractory Wear", *ISIJ International*, vol. 42, pp. 235-242.

He, Q., Zulli, P., Evans, G. M. and Tanzil, F. (2006), "Free surface instability and gas entrainment during blast furnace drainage", *Development in Chemical Engineering and Mineral Processing*, vol. 14, pp. 249-258.

He, Q., Evans, G., Zulli, P. and Tanzil, F. (2009), "Investigation of viscous fingering during blast furnace hearth drainage using a Hele-Shaw viscous flow model", Proceedings of the 5th International Congress on the Science and Technology of Ironmaking, Shanghai, China, pp. 1130-1134.

He, Q., Evans, G., Zulli, P. and Tanzil, F. (2012), "Cold model study of blast gas discharge from the taphole during the blast furnace hearth drainage", *ISIJ International*, vol. 52, pp. 774-778.

Houde, J. P., Hebel, R. and Dulz, V. (2013), "Comparison of different BF-hearth lining design technologies", Proc. 43rd Ironmaking and Raw Materials Seminar, 12h Brazilian Symposium on Iron Ore and 1st Brazilian Symposium on Agglomeration of Iron Ore, Belo Horizonte, MG, Brazil.

Iida, M., Ogura, K. and Hakone, T. (2008), "Analysis of Drainage Rate Variation of Molten Iron and Slag from Blast Furnace during Tapping", *ISIJ International*, vol. 48, pp. 412-419.

Iida, M., Ogura, K. and Hakone, T. (2009), "Numerical Study on Metal/Slag Drainage Rate Deviation during Blast Furnace Tapping", *ISIJ International*, vol. 49, pp. 1123-1132.

Inada, T., Kasai, A., Nakano, K., Komatsu, S. and Ogawa, A. (2009), "Dissection Investigation of Blast Furnace Hearth – 2nd Campaign", *ISIJ International*, vol. 49, pp. 470-478.

Jiao, K. X., Zhang, J. L., Liu, Z. J., Xu, M. and Liu, F. (2015), "Formation mechanism of the protective layer in a blast furnace hearth", *International Journal of Minerals, Metallurgy, and Materials*, vol. 22, pp. 1017-1024.

Jiao, K. X., Zhang, J. L., Liu, Z. J., Chen, C. L. and Liu, Y. X. (2016), *ISIJ International*, vol. 56, pp. 1956-1963.

Kanbara, K., Hagiwara, T., Shigemi, A., Kondo, S., Kanayama, Y., Wakabayashi, K. and Hiramoto, N. (1977), "Dissection of Blast Furnaces and Their Internal State", *Transactions of the ISIJ*, vol. 17, pp. 371-380.

Kaymak, Y., Hauck, T., Lin, R. and Rausch, H. (2017), "Simulation of Slag/Gas and Slag/Iron Interface Tilting in Blast Furnace Hearth during Slag Tapping", COMSOL Conf. 2017, Rotterdam, Netherland.

Kumar, S. (2005), "Heat Transfer Analysis and Estimation of Refractory Wear in an Iron Blast Furnace Hearth Using Finite Element Method", *ISIJ International*, vol. 45, pp. 1122-1128.

Lai, P. C., Du, S. W., Liu, S. H. and Cheng, W. T. (2021), "Numerical investigation on effects of cooling water temperature and deadman status on thermal flow in the hearth of blast furnace during tapping shutdown", *Thermal Science and Engineering Progress*, vol. 23, pp. 100908.

Liu, Z. J., Zhang, J. L., Zuo, H. B. and Yang, T. J. (2012), "Recent Progress on Long Service Life Design of Chinese Blast Furnace Hearth", *ISIJ International*, vol. 52, pp. 1713-1723.

Luomala, M. J., Mattila, O. J. and Härkki, J. H. (2001), "Physical modelling of hot metal flow in a blast furnace hearth", Scandinavian Journal of Metallurgy, vol. 30, pp. 225-231.

Mitra, T. and Saxén, H. (2014), "Model for Fast Evaluation of Charging Programs in the Blast Furnace", *Metallurgical and Materials Transactions B*, vol. 45, pp. 2382–2394.

Negro, P., Petit, C., Urvoy, A., Sert, D. and Pierret, H. (2001), "Characterization of the permeability of the blast furnace lower part", *Revue Métallurgie*, vol. 98, pp. 521–531.

Nightingale, R. J., Tanzil, F. W. B. U., Beck, A. J. G. and Price, K. (2001), "Blast furnace hearth condition monitoring and taphole management techniques", *Metallurgical Research & Technology*, vol. 98, pp. 533-540.

Nishio, H., Wenzel, W. and Gudenau, H. W. (1977). "The Significance of the Dead Zone in the Blast Furnace", *Stahl und Eisen*, vol. 97, pp. 867-875.

Nishioka, K., Maeda, T. and Shimizu, M. (2005a), "Effect of Various In-furnace Conditions on Blast Furnace Hearth Drainage", *ISIJ International*, vol. 45, pp. 1496-1505.

Nishioka, K., Maeda, T. and Shimizu, M. (2005b), "A Three-dimensional Mathematical Modelling of Drainage Behavior in Blast Furnace Hearth", *ISIJ International*, vol. 45, pp. 669-676.

Nouchi, T., Sato, M., Takeda, K. and Ariyama, T. (2005), "Effects of

Operation Condition and Casting Strategy on Drainage Efficiency of the Blast Furnace Hearth", *ISIJ International*, vol. 45, pp. 1515-1520.

Nouchi, T., Yasui, M. and Takeda, K. (2003), "Effects of Particle Free Space on Hearth Drainage Efficiency", *ISIJ International*, vol. 43, pp. 175-180.

Omori, Y. (Ed.) (1987) *Blast Furnace Phenomena and Modelling*, Iron and Steel Institute of Japan, Elsevier, London.

Park, J., Jung, H., Jo, M., Oh, H. and Han, J. (2011), "Mathematical modeling of the burden distribution in the blast furnace shaft", *Metals and Materials International*, vol. 17, pp. 485-496.

Post, J. (2019), *Simulation of the Inhomogeneous Deadman of an Ironmaking Blast Furnace*, Doctoral thesis, TU Delft, Delft, Netherlands.

Raipala, K. (2003), *On hearth phenomena and hot metal carbon content in blast furnace*, Doctoral thesis, Helsinki University of Technology, Helsinki, Finland.

Roche, M., Helle, M., van der Stel, J., Louwerse, G., Shao, L. and Saxén, H. (2018), "Off-line Model of Blast Furnace Liquid Levels", *ISIJ International*, vol. 58, pp. 2236-2245.

Roche, M., Helle, M., van der Stel, J., Louwerse, G., Shao, L. and Saxén, H. (2019), "On-Line Estimation of Liquid Levels in the Blast Furnace Hearth", *Steel Research International*, vol. 90, pp. 1800420.

Roche, M., Helle, M., van der Stel, J., Louwerse, G., Storm, J. and Saxén, H. (2020), "Drainage Model of Multi-taphole Blast Furnaces", *Metallurgical and Materials Transactions B*, vol. 51, pp. 1731-1749.

Roche, M. (2020), *Modeling and analysis of blast furnace drainage*, Doctoral thesis, Åbo Akademi University, Turku, Finland.

Saxén, H. (2015), "Model of Draining of the Blast Furnace Hearth with an Impermeable Zone", *Metallurgical and Materials Transactions B*, vol. 46, pp. 421-431.

Seetharaman, S. (2014), Treatise on Process Metallurgy, Volume 3: Industrial Processes, Part A, American Elsevier Company, New York, USA.

Shao, L. and Saxén, H. (2011), "A Simulation Study of Blast Furnace Hearth Drainage Using a Two-phase Flow Model of the Taphole", *ISIJ International*, vol. 51, pp. 228–235.

Shao, L. and Saxén, H. (2012a), "Numerical prediction of iron flow and bottom erosion in the blast furnace hearth", *Steel Research International*, vol. 83, pp. 878–885.

Shao, L. and Saxén, H. (2012b), "Model of Blast Furnace Hearth Drainage", *Steel Research International*, vol. 83, pp. 197–204.

Shao, L. (2013), *Model-Based Estimation of Liquid Flows in the Blast Furnace Hearth and Taphole*, Doctoral thesis, Åbo Akademi University, Turku, Finland.

Shao, L. and Saxén, H. (2013a), "A Simulation Study of Two-liquid Flow in the Taphole of the Blast Furnace", *ISIJ International*, vol. 53, pp. 988–994.

Shao, L. and Saxén, H. (2013b), "Simulation study of blast furnace drainage using a two-fluid model", *Industrial & Engineering Chemistry Research*, vol. 52, pp. 5479–5488.

Shen, Y., Shiozawa, T., Austin, P. and Yu, A. (2014) "Model study of the effect of bird's nest on transport phenomena in the raceway of an ironmaking blast furnace", *Minerals Engineering*, vol. 63, pp. 91-99.

Shibata, K., Kimura, Y., Shimizu, M. and Inaba, S. (1990), "Dynamics of Dead-man Coke and Hot Metal Flow in a Blast Furnace", *ISIJ International*, vol. 30, pp. 208-215.

Sugiyama, T. (1996), "Experimental and numerical analysis on the movement and the accumulation of powder in the deadman and the dripping zone of blast furnace", *Tetsu-to-Hagané*, vol. 82, pp. 29–34.

Takahashi, H., Kawai, H. and Suzuki, Y. (2002), "Analysis of stress and buoyancy for solids flow in the lower part of a blast furnace", *Chemical Engineering Science*, vol. 57, pp. 215–226.

Tanzil, W.B.U., Zulli, P., Burgess, J.M. and Pinczewski, W.V. (1984), "Experimental Model Study of the Physical Mechanisms Governing Blast Furnace Hearth Drainage", *Transactions of the ISIJ*, vol. 24, pp.197-205.

Tanzil, W.B.U. (1985), *Blast furnace hearth drainage*, Doctoral thesis, University of New South Wales, Sydney, Australia.

Torrkulla, J. and Saxén, H. (2000), "Model of the state of the blast furnace hearth", *ISIJ International*, vol. 40, pp. 438-447.

Tsuchiya, N., Fukutake, T., Yamauchi, Y. and Matsumoto, T. (1998), "In-furnace Conditions as Prerequisites for Proper Use and Design of Mud to Control Blast Furnace Taphole Length", *ISIJ International*, vol. 38, pp. 116-125.

Vångö, M., Pirker, S. and Lichtenegger, T. (2018), "Unresolved CFD–DEM modeling of multiphase flow in densely packed particle beds", *Applied Mathematical Modelling*, vol. 56, pp. 501–516.

Vats, A. K. and Dash, S. K. (2000), "Flow Induced Stress Distribution on Wall of Blast Furnace Hearth", *Ironmaking and Steelmaking*, vol. 27, pp. 123-128.

World Steel Association, World Steel in Figures 2010 to 2021. Available: https://www.worldsteel.org/steel-by-topic/statistics/World-Steel-in-Figures.html.

Yoon, H. S. and Park, K. M. (2021), "Behavior of the free surface of two-phase fluid flow near the taphole in a tank", *Symmetry*, vol. 13, pp. 875.

Yu, X. B. and Shen, Y. S. (2019), "Model Study of Blast Furnace Operation with Central Coke Charging", *Metallurgical Materials Transactions B*, vol. 50, pp. 2238-2250.

Zulli, P. (1991), *Blast furnace hearth drainage with and without a coke free layer*, Doctoral thesis, University of South Wales, Sydney, Australia.

ISBN 978-952-12-4155-0